NASA-CR-201532

NASA FLOW FIELD ANALYSIS

Charles L. Merkle
Department of Mechanical Engineering
The Pennsylvania State University
University Park, PA 16802

FINAL REPORT

Irene Cierchacki
Grants Officer
NASA Lewis Research Center
21000 Brookpark Road
Cleveland, OH 44135

Grant/Contract No. NAG3-1735

July, 1996

Objective

The objectives of the present research are to improve design capabilities for low thrust rocket engines through understanding the detailed mixing and combustion processes in a representative combustor. Of particular interest is a small gaseous hydrogen-oxygen thruster which is considered as a coordinated part of an on-going experimental program at NASA LeRC. Detailed computational modeling involves the solution of both the two- and three-dimensional Navier Stokes equations, coupled with chemical reactions and the species diffusion equations. Computations of interest include both steady state and time-accurate flowfields and are obtained by means of LU approximate factorization in time and flux split upwinding differencing in space. The emphasis in the research is focused on using numerical analysis to understand detailed combustor flowfields, including the shear layer dynamics created between fuel film cooling and the core gas in the vicinity on the nearby combustor wall; the integrity and effectiveness of the coolant film; and three-dimensional fuel and oxidizer jet injection/mixing/combustion characteristics in the primary combustor along with their joint impacts on global engine performance.

Progress to Date

The specific engine of interest is a small gaseous hydrogen-oxygen engine originally designed to provide auxiliary propulsion and attitude control for Space Station Freedom (see Fig. 1). This engine provides about 110 N (25 lbf) of thrust and uses the entire hydrogen gas flow for regenerative cooling after which about two-thirds of it is split off for wall film cooling while the remaining one-third is mixed with the oxidizer and used for primary combustion. The primary combustor for this engine is an Aerojet platelet design in which the fuel and oxidizer are injected through separate ports around the periphery of the core section. A second geometry that uses impinging injectors has recently been designed at NASA Lewis for this engine. A series of computational results have been obtained for the platelet configuration. In addition, preliminary attempts at obtaining solutions for the impinging injector have also been obtained. These results are described in the present report along with an assessment of the issues involved in modeling ethanol-oxygen spray combustion. We address these three topics in order, with primary emphasis on the platelet injector results.

Platelet Injector - Simplified Geometry - Hydrogen Crossflow

The geometry of the platelet injector is given in Fig. 2. The core combustor is on the left, while the area where the hydrogen cooling gas is introduced along the walls is further downstream. The figure also shows the spark plug that is used for ignition. Initially, it was expected that the bluff body region behind the spark plug would create a recirculation region that would ensure uniform mixing.

The hydrogen and oxygen are introduced through two axial stations into the core region A total of 12 radial ports is used for each propellant. The oxygen is introduced about halfway between the blind upstream end and the end of the spark

plug, while the hydrogen jets are at the downstream edge of the plug. The oxygen ports are clocked with respect to the hydrogen ports so that the oxygen jets enter between the hydrogen jets. Because of the platelet fabrication technique, the ports are rectangular in shape.

Initial modeling of this engine assumed that the multiple jets and the bluff body region downstream of the spark plug would result in excellent mixing so the core flow was assumed to produce ideal, uniform combustion and attention was directed toward the characteristics of the film cooling layer. As the film is convected through the engine between the injection plane and the throat, a fraction of it mixes with the oxidizer-rich core gases and burns. This combustion reduces the thickness of the coolant layer and weakens its effectiveness, but it also improves the overall efficiency of the thruster. These previous results included both steady and unsteady analyses. The results show that the mixing layer set up by the film coolant leads to an unsteady fluctuation in the mixing layer region, but this unsteadiness does not have a major effect on the amount of the film that is combusted.

Recent diagnostic measurements of the platelet injector have indicated, however, that a large amount of nonuniformity exists in the core region. Consequently, the assumption of uniform mixing and combustion is not appropriate. Accordingly, cold flow mixing in the core was started last year, and extended to combustion calculations during the present reporting period.

As a first step in these three-dimensional analyses of the core flow region, only the hydrogen jets were treated discretely while the oxygen flow was modeled as a uniform axial stream that entered through the upstream boundary as shown in Fig. 3. For computational efficiency, the domain of interest extended only to the end of the spline sleeve that meters in the film coolant. Some preliminary computations without the spark plug were done initially, but all results presented herein include the spark plug.

The computational domain for the computations with the uniform oxygen injection is shown in Fig. 3. As the figure shows, the hydrogen injection ports are just downstream of the end of the spark plug. The injection holes are rectangular with a size of 0.06" x 0.03". The propellant flow rates are chosen to match the experimental setup, with an overall mass flow rate of 0.0322 kg/s, an overall O/F ratio of 5.13, and 75% FFC. The hydrogen fuel is injected at 400 K while the core oxygen enters at 300 K. These flow rates result in a hydrogen injection speed of 325 m/s, and an oxygen core flow speed of 13 m/s.

Since the injector contains 12 hydrogen ports, we divide the entire combustor into 24 symmetric slices, each composed of a 15 degree angle of the cylindrical combustor. The computation is then performed on a single injector using symmetry conditions as shown in Fig. 4 to provide the solution for the entire primary combustor. The computational grid is given in Fig. 5. Fig. 5a shows the grid in the symmetry plane while Fig. 5b shows the grid in the cross-plane. The grid size chosen is 41 x 61 x 41. The grid is stretched near the injector port both in axial and azimuthal directions to provide resolution for the incoming hydrogen jet.

Prior to presenting the combustion results, we give an overview of the cold flow solution to provide perspective on the mixing. To show the three-dimensional effects, we use one-fourth of the combustor which involves three injection holes. Contours of the hydrogen concentration are given in three-dimensional view shown in Fig. 6. This plot shows the hydrogen concentration at the axial location where it enters from the side wall an at several locations downstream. The spark plug, represented by the shaded region, lies just upstream of the injection holes. As can be seen from this figure, each hydrogen jet bends rapidly toward the downstream direction and splits into two counter-rotating spiral vortices.

To provide more detail of the flow near the hydrogen jets, we present in Fig. 7 the velocity vectors and streamlines of a single injector slice for a cross-plane located 5 mm downstream of the injection port. The hydrogen jet induces two clearly observed counter-rotating vortices that are symmetric about the center plane of the injection hole. These vortices roll the oxygen to the top of the hydrogen jet and down inside its center portion, eventually splitting the hydrogen jet into two parts.

Corresponding cross-plane contour plots of the hydrogen mass fraction in the cold flow case are presented in Fig. 8 to better understand the detailed local mixing effects and flowfield characteristics. Four cross-plane locations starting from the symmetry plane of an injector port, followed by the edge of an injection port, a location between the edge of the injector and the injector slice symmetry boundary, and the injector symmetry boundary, are given to show variations in the x - r plane. Although the velocity of the hydrogen jet is much larger than that of the core oxygen flow (the velocity ration is 25), the momentum ratio between the two streams (H_2 to O_2) is only 1.5. The hydrogen penetrates approximately halfway to the axis of symmetry before being swept toward the streamwise direction by the oxygen core flow as shown in Figs. 8a, b, and c. In the injection port symmetry plane, only a limited amount of hydrogen exists near the combustor wall (Fig. 8a), because at this cross-plane, the oxygen rolls up and quickly diffuses into the middle of the jet because of the two counter-rotating horseshoe vortices.

At the edge of the injection hole (Fig. 8b), the hydrogen jet remains closer to the combustor wall, but some hydrogen still reaches the centerline as it also did in Fig. 8a. Both Fig. 8b and Fig. 8c show a region of high hydrogen concentration downstream of the spark plug. The cross-plane shown in Fig. 8c does not lie beneath the injection port, so this hydrogen concentration is the result of jet diffusion and expansion in the θ direction.

At the injector slice symmetry plane in Fig. 8d, the amount of hydrogen that exists near the spark plug tip is smaller as compared to Figs. 8a, b and c, because only a limited amount of hydrogen is able to diffuse this far to reach the injector slice boundary. Here, most of the hydrogen is near the top wall. These results clearly indicate that ideal mixing is not achieved in the cold flow case.

Corresponding results for the reacting flow case are given in Figs. 9 through 19. Figure 9 shows the three-dimensional hydrogen mass fraction contours over one quarter of the combustor, which again contains three injector ports. The spark plug

is again represented by the shaded region. As in the cold flow case, each hydrogen jet is turned toward the streamwise direction, split into two lobes and then merges with the adjacent lobe. In contrast to the cold flow solution shown in Fig. 6, the hydrogen is completely burned about half way through the primary combustion zone and no contours are visible past this point.

Representative cross-sectional plots of the velocity vectors at five axial locations behind a single injector (a 30 degree sector) are plotted in Fig. 10 to demonstrate the effect of the horseshoe vortices in the combustion case. These five axial locations are 5 mm, 10 mm, 20 mm, and 30 mm downstream of the injector port, as shown schematically in Fig. 11. The counter-rotating vortices induced by the hydrogen jet as it is injected into the chamber can be seen in Fig. 10a. As the jet travels downstream, these vortices grow in size as seen from Figs. 10b, c, and d, but their strength starts to decay because of dispersion. Figure 10e shows the remnants of these vortices at the end of the primary combustor just before the flow enters the wall cooling section of the chamber (30 mm downstream of the injector port). These vortices may enhance mixing and combustion of the hydrogen film coolant in the wall shear region, but three-dimensional computations have not been extended into this region.

A series of θ cross-plane contour plots for hydrogen mass fraction are shown in Fig. 12. These four cross-planes are chosen at the same positions as those in Fig. 8. Figures 12a and b show that the hydrogen penetrates only about 5 mm into the oxygen core before being swept toward the axial direction by the oxygen core flow. In contrast to the cold flow solutions, no hydrogen reaches the centerline. Thus, the presence of combustion is seen to decrease the jet penetration distance, and the flame quickly consumes the incoming hydrogen jet. All the hydrogen is consumed at an axial location 20 mm downstream of the injector port. The azimuthal plane in Fig. 12c has no hydrogen injection, but still contains a significant amount of hydrogen, but only a small amount is able to reach the symmetry plane between the injectors as shown in Fig. 12d. All four plots in Fig. 12 show that the hydrogen is consumed before the end of the primary combustor is reached. Comparison of Fig. 12 with Fig. 8 shows the dramatic differences between the reacting and cold flow solutions.

Cross-sectional contour plots of the hydrogen mass fraction at the five axial locations shown previously (Fig. 10) are given in Fig. 13. Figure 13a shows the penetration of the jet at the injection plane, while Figs. 13b and c show the two lobes of the jet as it is split by the counter-rotating vortices, and the decreased concentration because a portion of the hydrogen has been burned. Beyond the 20 mm location (Figs. 13d and e), the hydrogen is nearly completely burned.

The characteristics of the flame are best deduced from the concentrations in the θ and axial planes in Figs. 14 and 15 respectively. The location and outline of the spark plug is indicated in Fig. 15 by means of a zero OH contour line. The contours in Fig. 14 also indicate that the OH radical concentration inside the hydrogen jet where combustion has not yet occurred is zero, but that there are very steep OH concentration gradients near the edges of the jet.

For the inside boundary of the jet (closest to the centerline), the gradient first causes the OH concentration to rise to a maximum and then to drop rapidly back to zero. The OH concentration near the centerline then remains near zero at all locations. The maximum on the lower edge of the hydrogen jet clearly represents the location of the diffusion flame.

The steep OH gradient on the upper side of the hydrogen jet is somewhat different in that the OH concentration here rises to a maximum and remains there over a relatively large region near the wall. This large region of high OH radical concentration corresponds to a region of burned and burning gas. This region is affected by the mixing produced by the counter-rotating horseshoe vortex pair. An exception to this is the symmetry plane in Fig. 14d where the double steep gradient surrounds the hydrogen jet on both the bottom and the top.

The OH radical concentration in the axial plane in Fig. 15 show that burning continues as the jet convects downstream. At both the 20 mm and 30 mm axial locations, the OH radical mass fraction is above 0.12 in this region, indicating that these are high temperature flame zone regions that show the hydrogen jet is burned. The OH radical again has zero concentration near the centerline indicating the hydrogen jet is not able to penetrate this far.

Corresponding plots for the water vapor contours and for the temperature are given in Figs. 16, 17, 18 and 19. In general, these quantities provide information analogous to that given above. Additional results and discussion are given in Ref. 1.

Platelet Injector - Hydrogen and Oxygen Cross-Stream Injection

Both the cold flow and the hot flow results presented above are for the simplified geometry in which oxygen is injected from the upstream end and only the hydrogen enters through cross-stream jets (see Fig. 3). Computations for which both propellants are injected through all ports have also been computed and are presented next. The geometry for this computational configuration is given in Fig. 2 and is identical to the experimental geometry. The emphasis in the following discussion is on a comparison between the differences generated by the two oxygen injection methods. For this comparison, some of the results for the simplified geometry discussed above have been re-plotted and are presented again.

For the computations with cross-stream injection of both propellants, the oxygen is injected at an axial location near the curved region of the spark plug contour (not shown for simplicity in Fig. 2) 0.59" from the upstream end of the combustor. Each oxidizer injection hole is 2.03 mm x 2.03 mm (0.08" x 0.08") in area. The hydrogen fuel is injected into the chamber just downstream of the end of the spark plug, staggered at an angle of fifteen degrees with respect to the tangential location of the oxygen jets again as shown in Fig. 2. Each fuel injection hole is 1.52 mm x 0.76 mm (0.06" x 0.03") in area. The center of the hydrogen port is located 20 mm (0.78") from the upstream end of the combustor and about 2 mm (0.078") from the end of the spark plug. The overall mass flow rate is 0.0322 kg/s (0.0146 lbm/s), and the

overall O/F ratio in the primary combustor is 20.5 which is identical to that used in the computations for the simpler geometry.

To demonstrate the overall character of the reacting flow solutions, we begin by visualizing the hydrodynamic nature of the combustor flow. The velocity vectors along a tangential plane bisecting a hydrogen jet (θ location – see Fig. 2) are shown in Fig. 20a for the simplified case of transverse hydrogen injection into an axial oxygen flow. The hydrogen jet penetrates approximately one-fourth of the distance to the centerline before being swept downstream by the momentum of the core gas. A weak recirculation region is also established behind the igniter system protuberance. The velocity vectors for the case utilizing both transverse hydrogen and oxygen injection are shown in Fig. 20b along the identical tangential plane. The hydrogen penetration distance in this plane is drastically reduced when compared to the counterpart hydrogen fuel jet case shown in Fig. 20a because of interactions with the upstream oxygen jets. The velocity vectors along a tangential plane bisecting an oxygen jet (θ location 15° staggered with respect to hydrogen jets) demonstrate the oxygen jet behavior in Fig. 20c. The momentum of the oxygen jet is sufficient to penetrate through the low speed axial gas flow such that the jet impinges directly on the spark plug assembly. This splits the jet into two portions moving in opposite directions. The backward motion establishes a strong recirculation zone between the spark plug and the outer wall, and the forward moving portion induces a recirculation region behind the spark plug assembly. For this cross section, a fan region emerges near the hydrogen jet as a result of recirculating gases from the oxygen striking it.

Figure 21 shows the streamlines and velocity vectors for the transverse hydrogen and oxygen injection case for tangential wedge cross sections at a fixed axial location (see Fig. 2) along the combustor length. A single wedge is shown because the flowfield is periodic between each oxygen jet. At the axial location bisecting the hydrogen jet (x/L=0.4) shown in Fig. 21c, the upstream oxygen flow impinges directly on the center of the hydrogen jet, creating a fan region and breaking the hydrogen into two distinct lobes. At an axial location approximately 5 mm downstream (x/L=0.5) shown in Fig. 21b, several strong vortices are produced from a combination of the hydrogen/oxygen jet interaction and the recirculation region behind the igniter assembly. This should result in improved mixing and combustion performance. Figure 22 shows the streamlines and velocity vectors for the counterpart geometry using only transverse hydrogen injection into an axial oxygen flow. At the location of the hydrogen jet shown in Fig. 22a, the flow penetrates unobstructed into the chamber, forming two large symmetric counter-rotating vortices which are evident downstream in Fig. 22b. Note that the vortical nature of this flowfield is dramatically different than that predicted by the multiple jet injection case.

Figures 23 and 24 present similar cross-sections plots of OH concentrations at three axial locations. These are used as an indicator of flame location and character. Contour plots of the OH mass fractions in the three θ planes are given for: the symmetry plane of the hydrogen jet, 5 mm downstream from the hydrogen jet, and near the combustor exit plane. Figure 23 demonstrates the results for the case using both hydrogen and oxygen injection, and Fig. 24 presents the hydrogen

jet/axial oxygen flow case. In the mid-plane of the hydrogen injector port shown in Fig. 23a, there is very clear evidence that each hydrogen jet starts to react immediately after it enters the combustor indicated by the high OH concentration regions surrounding the jet. This is similarly true for the case in Fig. 24a, although the flame shape differs significantly in the previous case due to the oxygen jet interactions described earlier. At x/L = 0.5 or 5 mm downstream in the multiple jet case (Fig. 23b), two lobes of burned hydrogen are demonstrated by the OH concentrations in the central region. The flame region has also been diffused significantly downward toward the centerline of the combustor, likely as a result of the strong vortical nature of the flowfield shown earlier in Fig. 21. This is again true for the hydrogen jet/axial oxygen flow case shown in Fig. 24b, although a strong core region exists where no OH is present. This is a reflection of the hydrodynamic flowfield and the horseshoe vortices induced by the hydrogen jet. At the end of the primary combustor (Figs. 23c and 24c), the hydrogen jet is totally combusted and the OH mass fraction contours are relatively uniform for both cases. Similar investigation of the hydrogen contours (not shown) indicates all of the hydrogen burns in the oxygen rich combustor, but as the temperature contours given next indicate, the combustor does not provide the desired, uniform, well-mixed flowfield at the outlet.

The temperature contours for transverse hydrogen and oxygen injection at two tangential planes are shown in Figs. 25a and b. Figure 25a shows the tangential plane bisecting a hydrogen jet (see Fig. 2), and Fig. 25b presents the plane bisecting a oxygen jet (θ location 15° staggered with respect to hydrogen jets). The flame zone is established as the hydrogen is injected into the domain and convected downstream. The primary combustion zone is at approximately the flame temperature and is established near the wall of the chamber, and extends more toward the centerline as the flow is mixed downstream by the jet horseshoe vortices and the igniter recirculation zone. Similar contours at identical locations are shown for only transverse hydrogen injection in Figs. 25c and d.

The corresponding temperature contours in Figs. 25a-d clearly show that a large region of cold flow remains near the centerline. Inspection of other flowfield results verifies that this central core region contains a large fraction of unmixed, unreacted oxygen. This cold core region extends from the centerline to about one-third of the way to the combustor wall. Because of the geometry, this corresponds to just over 10% of the area, but, with a temperature of less than 1000 K as compared to the 3400 K temperature in the outer region, this small area contains almost one-third of the mass flow. This constitutes a very strong non-uniformity at the exit plane, and one that will probably traverse through the entire engine without mixing or reacting. Thus, although this design was expected to provide a very well-mixed, uniform outlet profile, the detailed CFD results suggest that a large fraction of the oxygen traverses through the combustor without mixing or reacting. Thus, all the hydrogen is mixing and reacting with the outer two-thirds of the oxygen, and even though full combustion is attained, the temperature in the outer annulus near the wall is hotter, requiring an increased amount of hydrogen fuel coolant downstream of the primary where the flow expands through the nozzle throat.

Mass-averaged cross-stream temperature and species profiles are given in Figs. 25 and 27 as a function of the radial coordinate for both geometries and are compared with experimentally measured values. These are averaged values over the θ variations in the flowfield at the combustor exit. These global parameters can then be compared with available experimental data for this engine. The results for averaged temperature are given in Fig. 26 reflect the cool oxygen core region indicated in the temperature contours presented earlier for both operating geometries. The averaged temperature for both the transversely injected hydrogen and oxygen and the transverse hydrogen jet cases are approximately 3400 K for radii greater than approximately 4 mm, indicating a full combusted condition in the upper portion of the chamber. The mass-averaged species mass fractions are shown in Fig. 27, and again reflect the oxygen core near the centerline. Both operating geometries reflect different trends in species concentration than the experimental results, although global trends are captured. In general, the upper portion of the combustor reflects the presence of significant combustion products, although more oxygen appears to be present in the multiple jet injection case, possibly as a results of increased mixing due to stronger vortical nature of the flowfield. Discrepancies in the results reflect the full three-dimensional nature of the flowfield at the combustor exit, and the difficulty in making comparisons with single line of experimental data on a given tangential plane. Inherent biases due to inhomogeneities in the axial velocity field also affect the averaging procedure.

Impinging Gas-Gas Injector

Preliminary work on an impinging injector for this same 110 N engine has also been initiated. A new injector design of this type has recently been fabricated for the engine shown in Fig. 1, and initial attempts at computing the flowfield in this configuration have been started. This impinging injector was designed by researchers at Lewis. A schematic of the injector is given in Fig. 28. As the figure shows, the oxygen enters axially through a single central jet while the hydrogen enters through four smaller jets at an angle with the oxygen jet (see Fig. 28).

An initial attempt at a grid is shown in Fig. 29. The grid plane shown is in the θ-plane that bisects the hydrogen jet. For expedience in grid representation, the hydrogen jets have been represented as "rectangular" elements in the O-grid on the end wall (circular arcs on top and bottom and radial rays on the two sides).

Representative axisymmetric solutions for this geometry (with the hydrogen entering through an annular slot instead of through four holes) are shown on Figs. 30 and 31. Figure 30 shows the temperature contours while Fig. 31 shows the OH contours. Note that in the annular slot configuration, the hydrogen jet does not penetrate to the center, and a cold, oxygen rich core is left. The four jets are expected to penetrate further because of the increased velocities they will have (since the same mass flows enters through a much smaller total area). The axisymmetric results do show that the flame begins right at the hydrogen injection port. Since the injector is a slot, combustion exists on only one side of the jet (oxygen cannot get between the hydrogen jet and the wall). Also note that the hot zone at first gets thinner with distance from the injection plane before starting to

thicken. This suggests that the flame is nearly quenched in this area and may represent a potential difficulty in flame-holding (at least in the computation). The thicker region further downstream may also represent a second flame-holding location near the impingement point. Again, this axisymmetric configuration lacks the 3-D relief effects that occur in the real (3-D) injector.

Attempts at extending this axisymmetric geometry to three-dimensions by closing part of the annular slot to form four injection ports have been started with both cold flow and hot flow computations. Thus far, these efforts have failed to lead to convergence. The main issue is finding an appropriate initial condition that will lead to convergence. This process has been hindered by the computational requirements for the reacting 3-D problem. Another possible difficulty may be that no steady solution exists but that the hydrogen jets flap in time and in this manner preclude convergence. Obtaining a solution appears straightforward, but requires additional efforts. Finally, we note that the chosen grid is still rather coarse to enable the problem to fit on a single workstation. We have access to parallel machines, but it is preferable to conduct exploratory calculations like the present one on single workstations to obtain the initial solution for a new problem. Finally, we also note that continued grid refinement in realistic combustion problems invariably results in an unsteady solution rather than a steady one. The present problem would not appear to be different. It is expected that this impinging ejector will be unsteady if the grid is made fine enough. We do, however, note that combustion heat release typically stabilizes the flowfield somewhat as compared to a cold-flow computation in the same geometry.

GOX-Ethanol Spray Combustion

The third and final topic concerned methods needed to compute GOX-ethanol spray combustion. The steps involved in modeling a liquid fuel with a gaseous oxidizer have been assessed and a method of approach has been formulated. The only actual computations with spray combustion that have been done have been for liquid oxygen with gaseous hydrogen. These, however, are sufficient to indicate that useful results can be obtained which will provide meaningful engineering insight. The steps completed are summarized below.

The kinetics of any hydrocarbon fuel are exceedingly complex. Current detailed reaction kinetics for methane involve some 50 species and 200 reactions. The number of species and reactions for ethanol would be much larger than for methane. This complexity precludes all but exploratory research computations of simple hydrocarbons with detailed kinetics. (Such computations are, however, possible, and we are pursuing a detailed CH_4-O_2 computation under other funding.) Reduced kinetic mechanisms and global one- or two-step mechanisms are, however, also available and are quite appropriate in two-dimensions The authors have used an approximate global mechanism for RP-1, and similar steps are easily accomplished for ethanol.

In terms of spray combustion, we have made considerable progress with LOX-hydrogen. Our approach is Lagrangian in nature and tracks a large number of

representative drops. Key issues in spray combustion computations are the definition of initial drop size and velocity distributions. Computational resources dictate that these atomization effects be supplied from simple correlations or direct experimental measurements. There are no theories available that are sufficiently advanced to predict drop distributions in configurations of interest. Another major issue is the potential differences between cold-flow atomization (where a large amount of data is available) and atomization in the presence of combustion (where almost no data is available).

Flame-holding also is an important issue in spray combustion computations. The indications are that small droplets contribute much to flame-holding, while the larger droplets dictate the major characteristics of the flame. When small drops are omitted, the flame may anchor at the wrong location (or for the wrong reason) and thereby distort the entire flame shape. Similarly, when large drops are omitted, the global burnout characteristics are altered. Thus, it appears important to retain a complete (and generally wide) droplet distribution. The use of a droplet distribution (as opposed to a single drop size) also increases the number of drops needed to obtain statistically meaningful results.

Appropriate interaction between a Lagrangian liquid phase and an Eulerian gas phase requires additional considerations. We have been able to obtain results that appear meaningful, but additional work is needed to identify the most efficient paths for reaching convergence simultaneously in both the liquid and gas phases, or even methods for verifying how well converged the results are. These are relatively mundane and simple tasks, but are ones that should be addressed.

Important effects that can be studied with spray combustion models include the manner in which the drop size changes with axial distance, both in terms of mean size (such as Sauter mean), or the size distribution function. In addition, effects of changes in the drop size on the overall flame characteristics can be studied. Initial results (in LOX-hydrogen) indicate the global flame characteristics are relatively insensitive to changes in the mean droplet size, but additional detailed study of the flame-holding mechanism must yet be completed.

Summary

Three-dimensional computations of the Aerojet platelet injector have been successfully completed. The results show the core flow region of the engine contains significant non-uniformities, and that there is, in particular, a cool, oxygen-rich region in the shadow of the spark plug. Extension of these computations through the entire combustor to the nozzle have not yet been attempted, but are important to see how well these three-dimensional striations mix by the time they reach the throat.

These computations are rather compute-intensive, and are stretching the capability of current workstations. Nevertheless, they are possible, and become more so with each workstation upgrade. Computations on parallel machines (with from 8 to 32 processors) would be reasonably efficient, but it continues to be difficult

to get the necessary CPU allocations to run these cases practically (8 processor machines would require about four days while 32 processors would require approximately 24 hours). Single workstations appear to be able to provide enough computational results to interact effectively with an experimental research program.

Attempts at obtaining solutions to the impinging injector problem have thus far been unsuccessful, but a careful methodical approach should be able to remedy this. Turnaround remains a major issue, but substantial progress can be made at a relatively low level.

Formulation of the ethanol-GOX spray combustion problem has also been addressed. Companion experimental-computational studies in this area would appear to be very timely. The computations need experimental insight to be sure they describe the physics properly, while the computational results should provide more insight to the experimental measurements. At the present time, it does not appear practical to predict drop size or even its evolution in the computational code. Finally, incorporation of a drop size distribution is important in spray combustion, and details of flame anchoring must be reproduced qualitatively to get the overall flame structure correct.

References and Publications

1. Tsuei, H.-H., "Computational Fluid Dynamic Modelling of Reacting Flowfields in Rocket Engines," Ph.D. Dissertation, The Pennsylvania State University (Department of Mechanical Engineering), University Park, PA, 1995.

2. de Groot, W. and Tsuei, H.-H., "Gaseous Hydrogen/Oxygen Injector Performance Characterization," AIAA Paper 94-0220, Reno, NV, 1994.

3. Tsuei, H.-H. and Merkle, C., "Mixing and Reaction in a Combustor With Transverse Jet Injection," AIAA Paper 95-0553, San Diego, CA, 1995.

4. de Groot, W. and Weiss, J., "Species and Temperature Measurements in H_2/O_2 Rocket Flowfields by Means of Raman Scattering Diagnostics," AIAA Paper 92-3353, Nashville, TN, 1992.

5. Grenda, J.M., Merkle, C.L., and Tsuei, H.-H., "Computational Procedure for Three-Dimensional Combustor Flowfield Analysis in Gas-Gas Rocket Engines," JANNAF Joint Meeting/Seventh Annual Propulsion Engineering Research Center Symposium, Huntsville, AL, October 23-27, 1995.

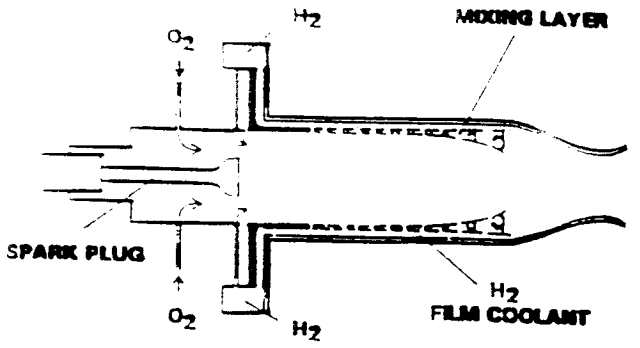

Figure 1: Schematic of the geometry of the gas/gas hydrogen/oxygen auxiliary rocket thruster.

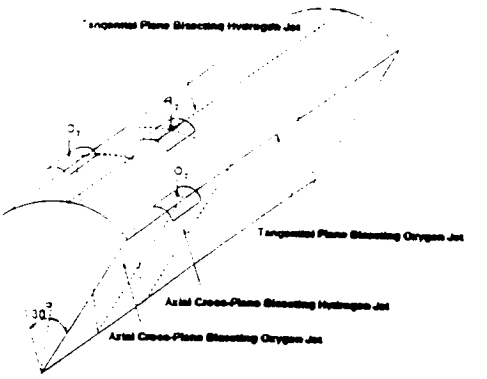

Figure 2: Three-dimensional schematic of the computational domain showing staggered location of oxygen and hydrogen jets.

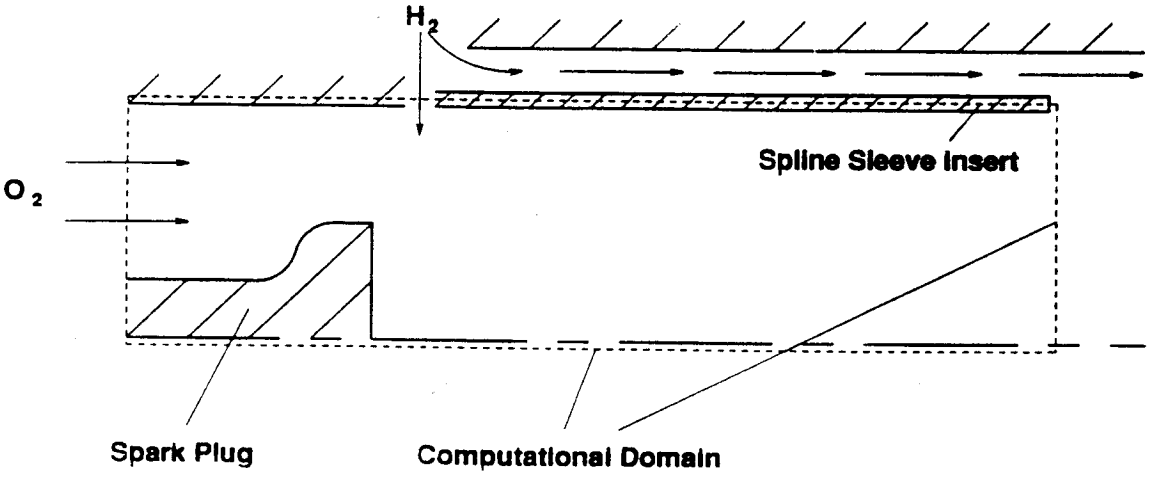

Figure 3: Schematic for an injector symmetry plane in the primary combustion zone of the Aerojet thruster: a. Combustor geometry; b. Computational model.

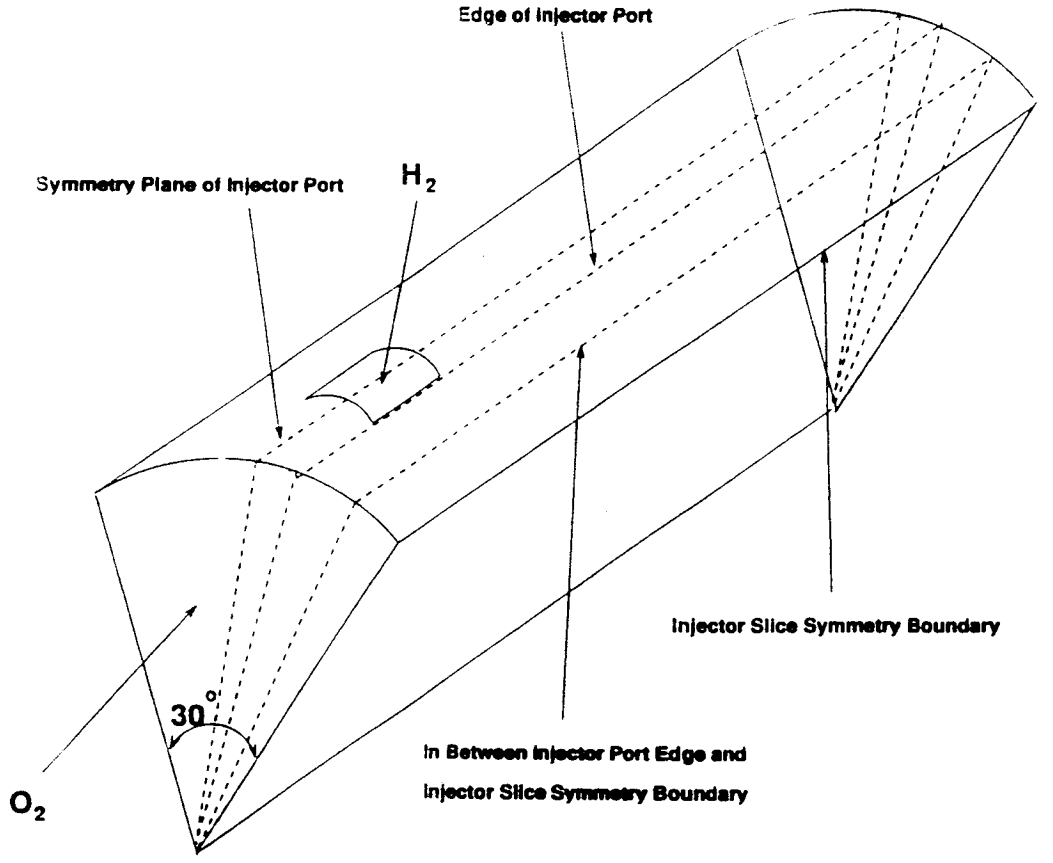

Figure 4: Schematic of a series of cross-planes in the θ direction.

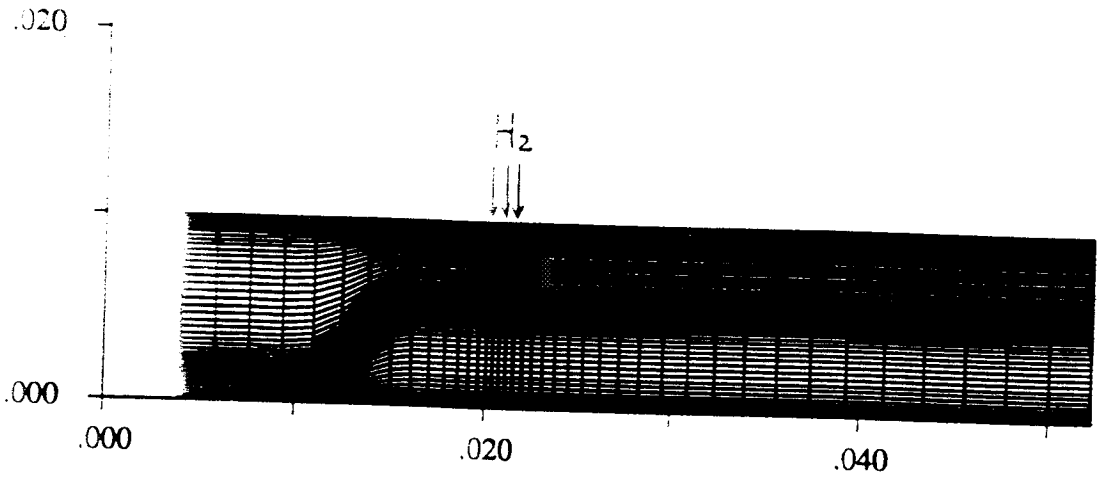

a.

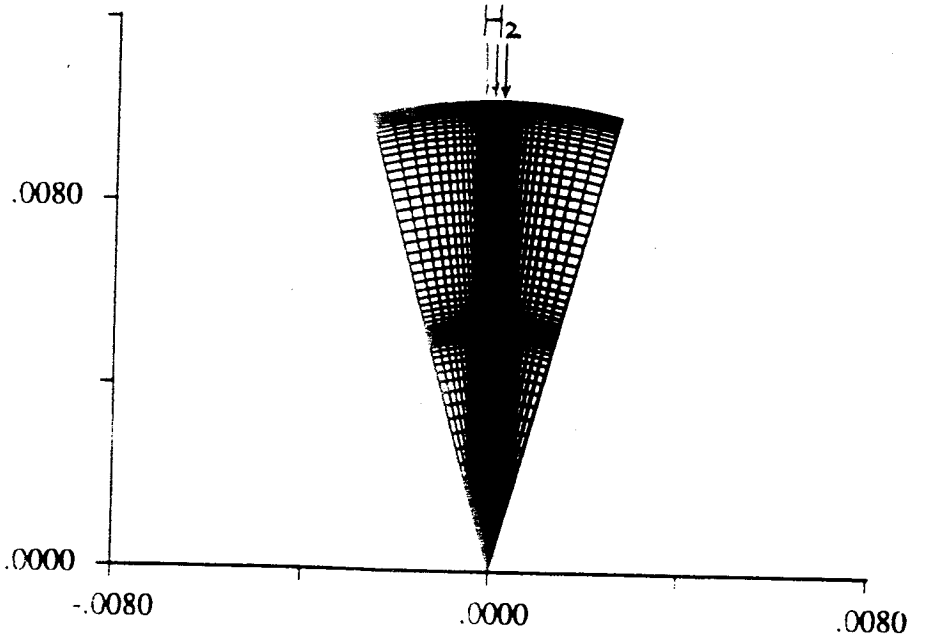

b.

Figure 3: Computational grid for the primary combustion zone: a. Injector symmetry plane; b. Cross-section view. The grid size is 41 x 61 x 41 for each injector slice.

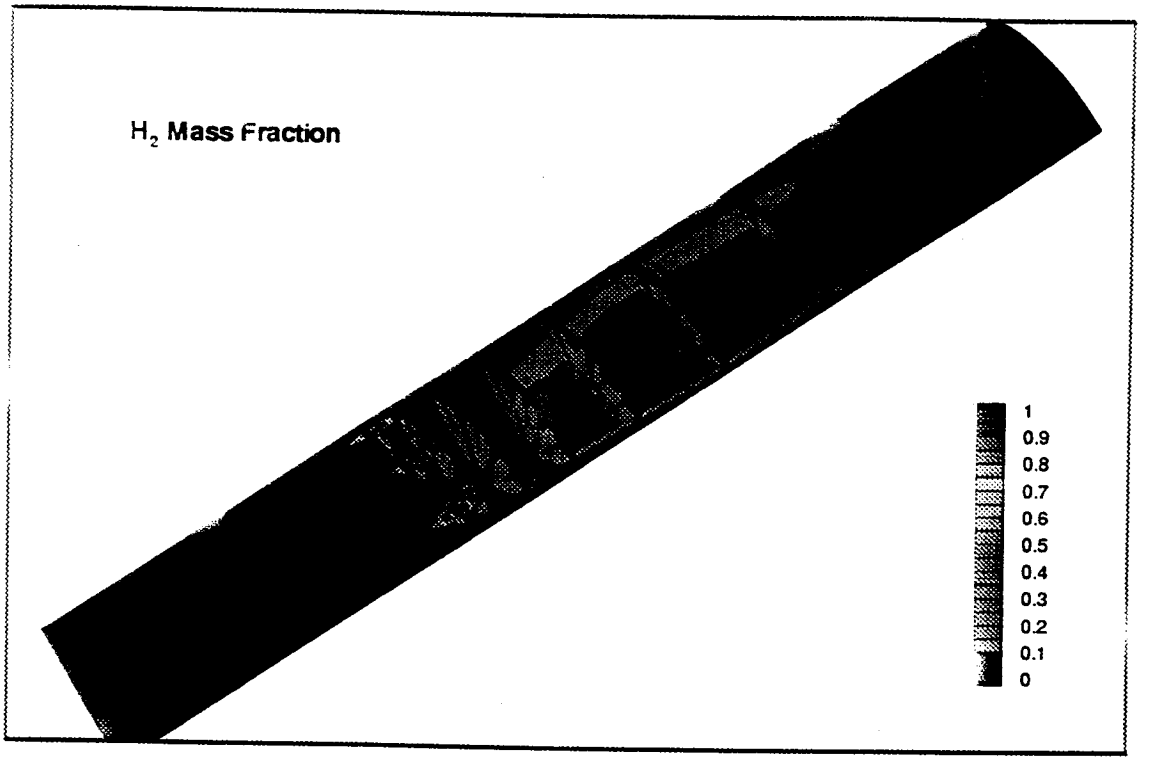

Figure 6: Hydrogen mass fraction contours in one-quarter of the combustor. The spark plug is represented by the shaded region.

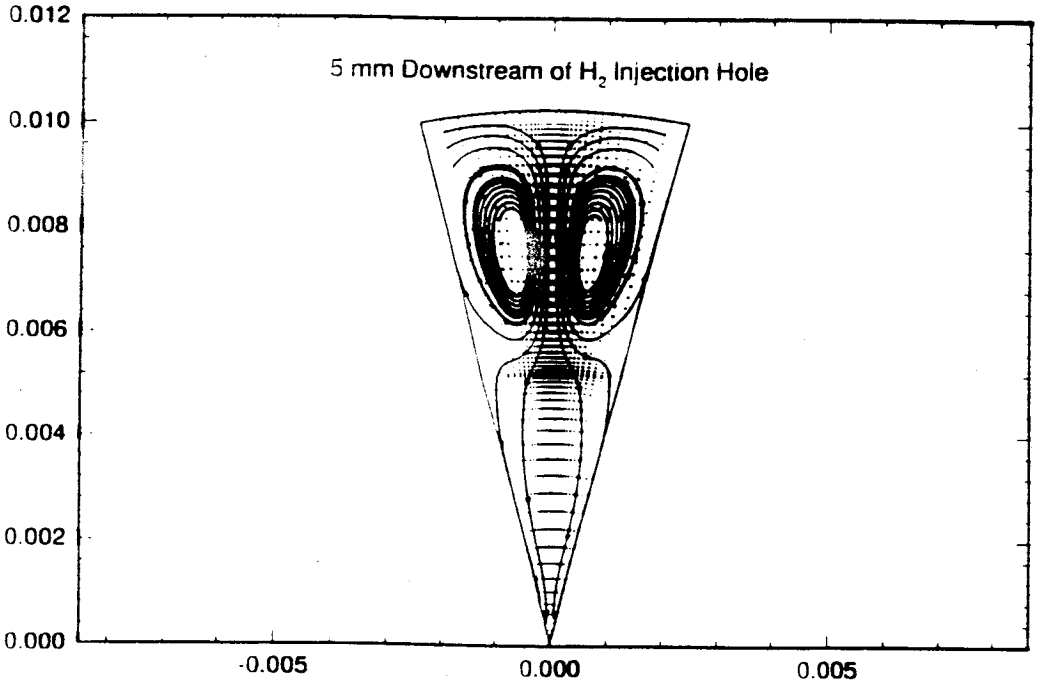

Figure 7: Velocity vectors and streamlines of a single injector slice cross-plane 5 mm downstream of the injector port.

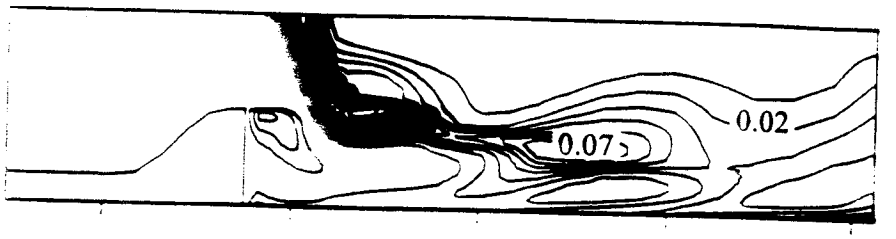

a. Symmetry plane of injector port

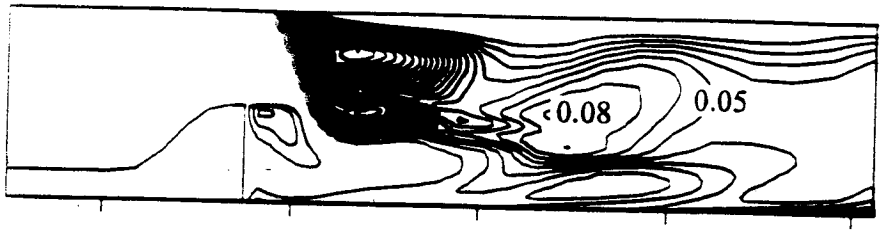

b. Edge of the injector port

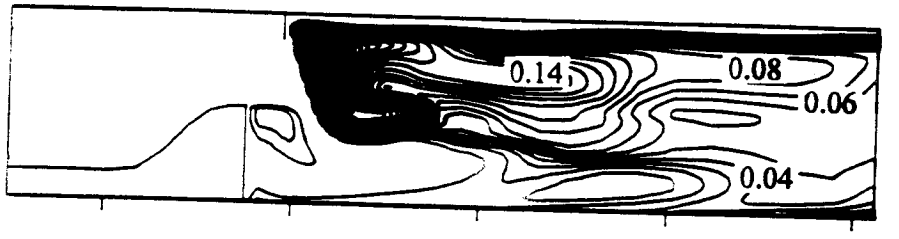

c. Between the injector edge and the injector slice symmetry boundary

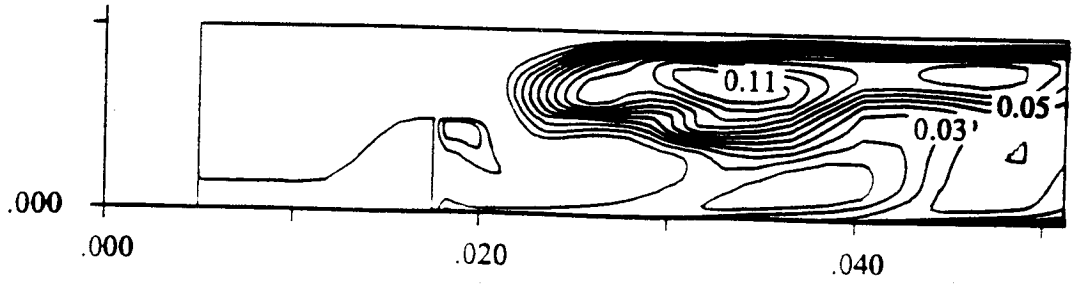

d. Injector slice symmetry boundary

Figure 5: Hydrogen mass fraction contours for a series of θ cross-planes.

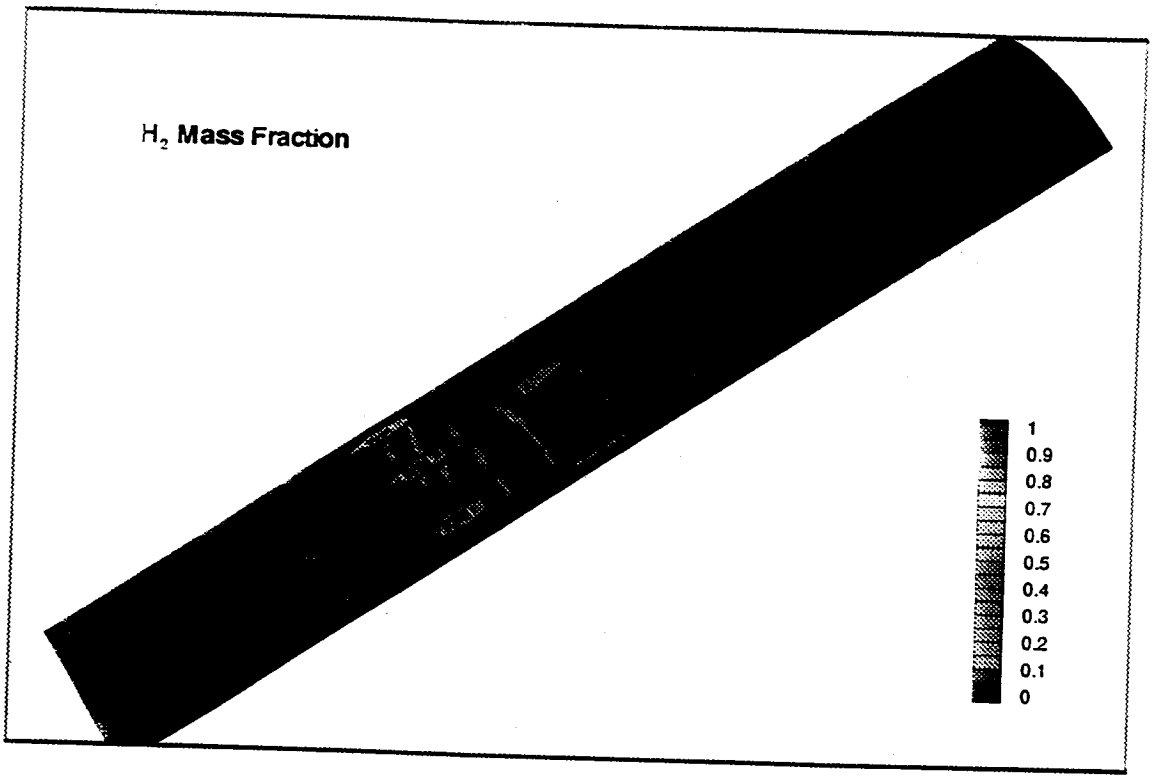

Figure 9: Hydrogen mass fraction contours in one-quarter of the combustor. Reacting Flow Solution. The spark plug is represented by the shaded region.

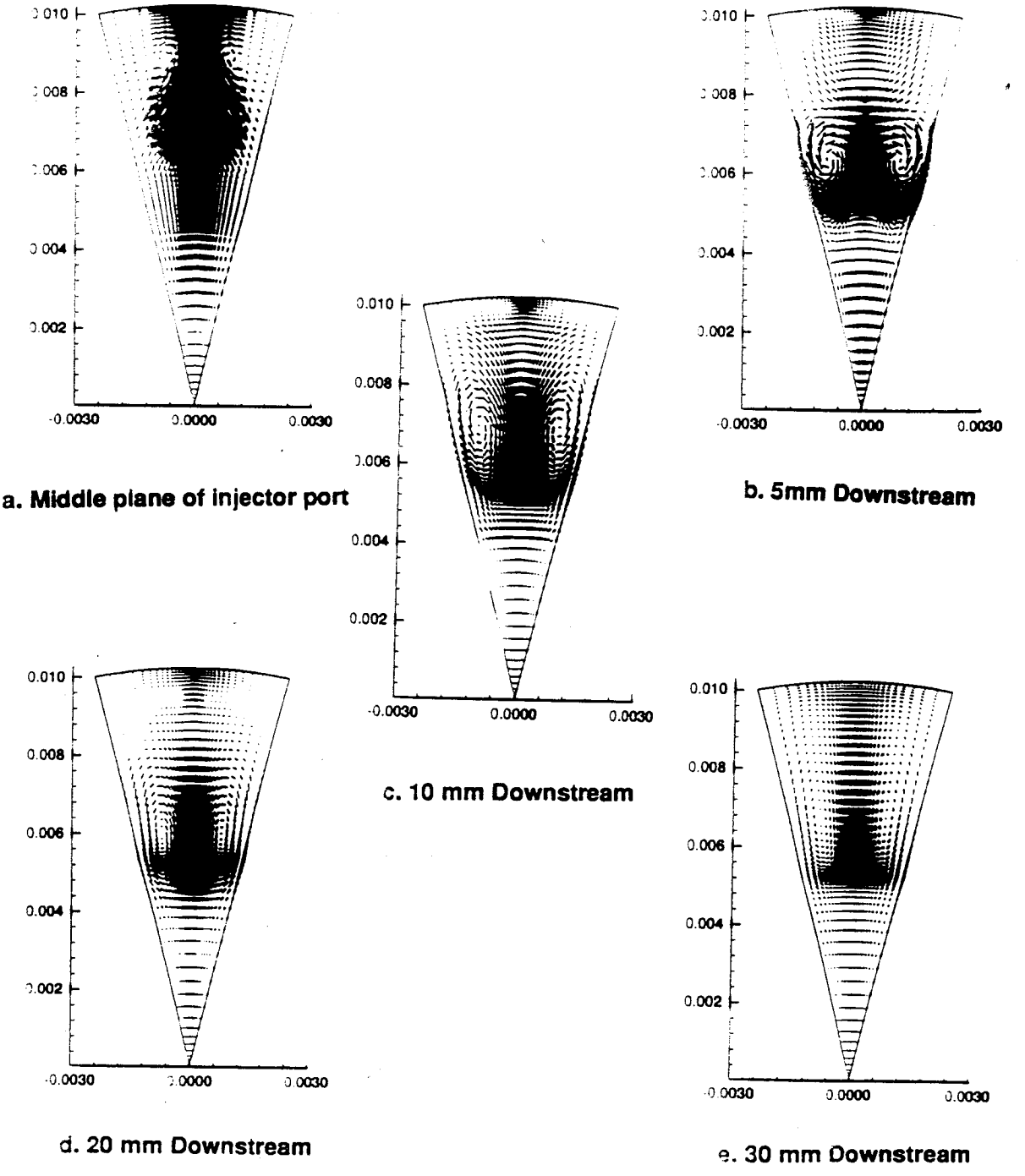

Figure 10: Velocity vectors at five axial cross-sections.

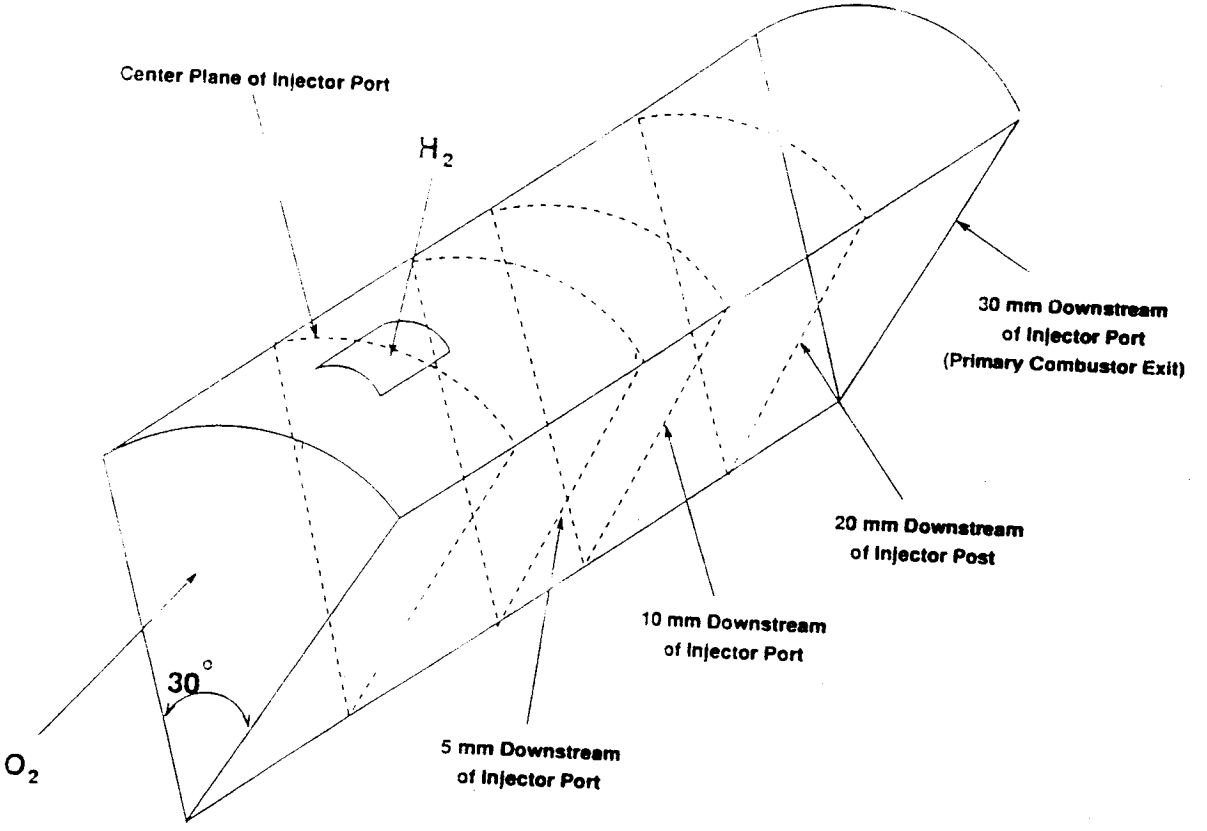

Figure 11: Schematic of a series of cross-sections in the axial direction.

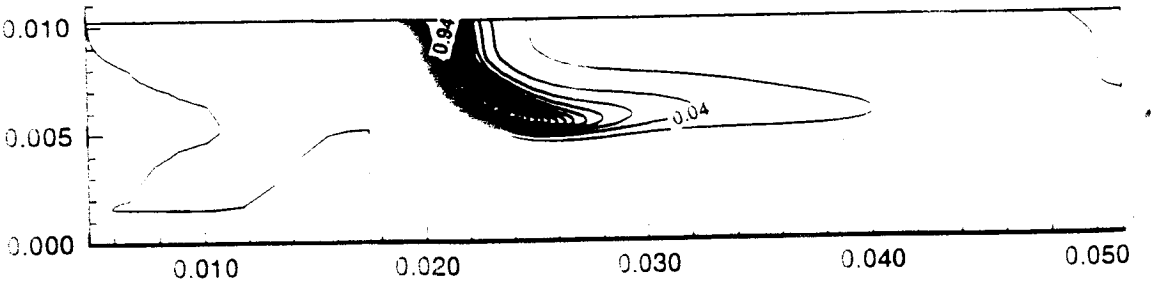

a. Symmetry plane of injector port.

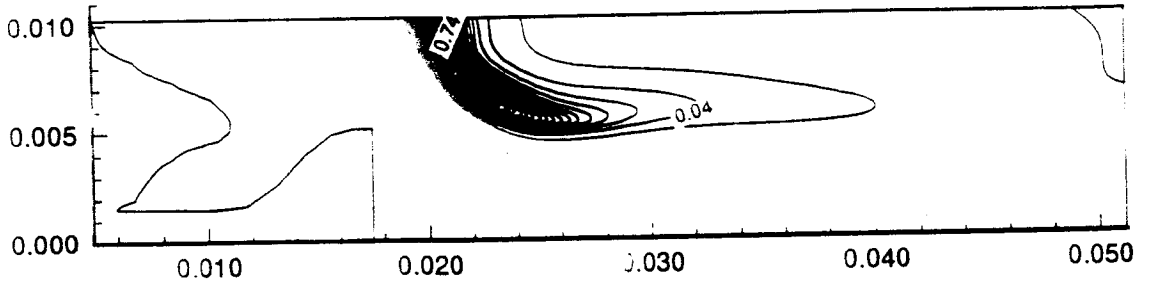

b. Edge of injector port.

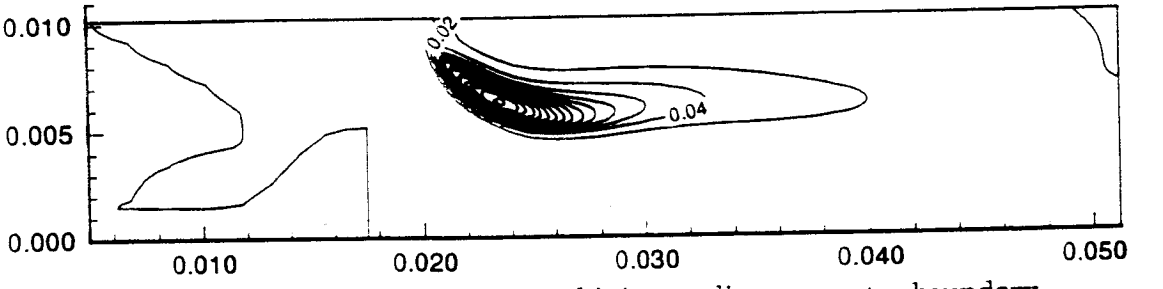

c. Between edge of injector port and injector slice symmetry boundary.

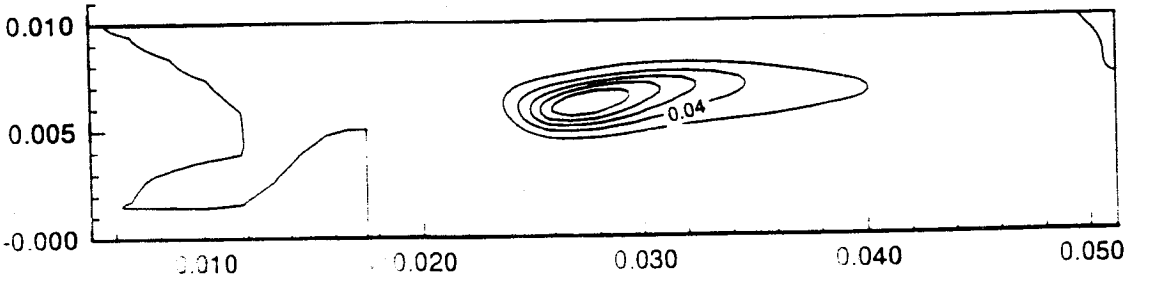

d. Injector slice symmetry boundary.

Figure 12: Hydrogen mass fraction contours for a series of θ cross-planes.

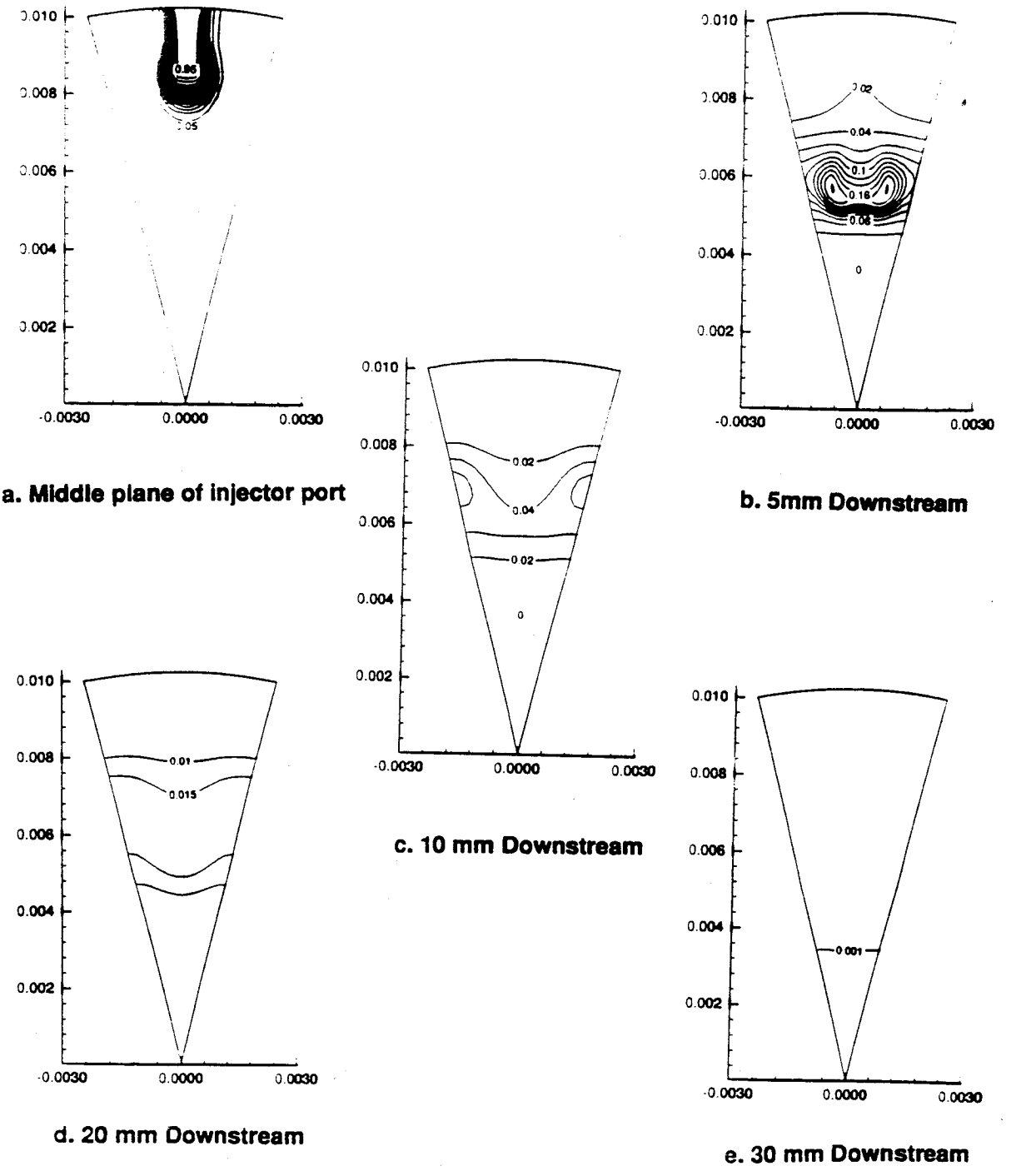

Figure 13: Hydrogen mass fraction contours at five axial cross-sections.

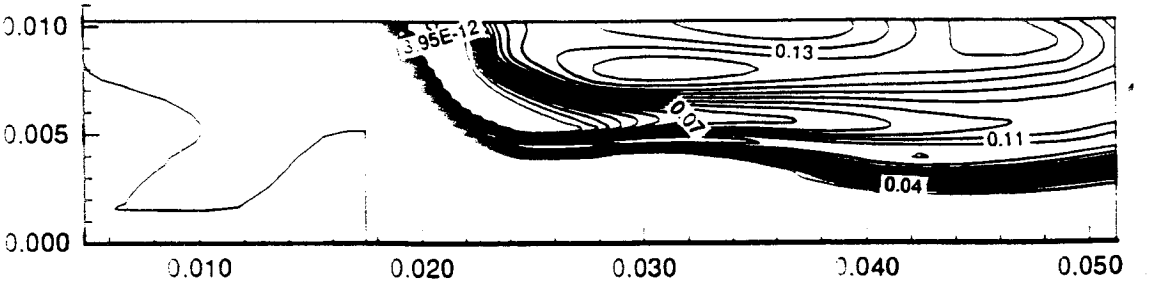

a. Symmetry plane of injector port.

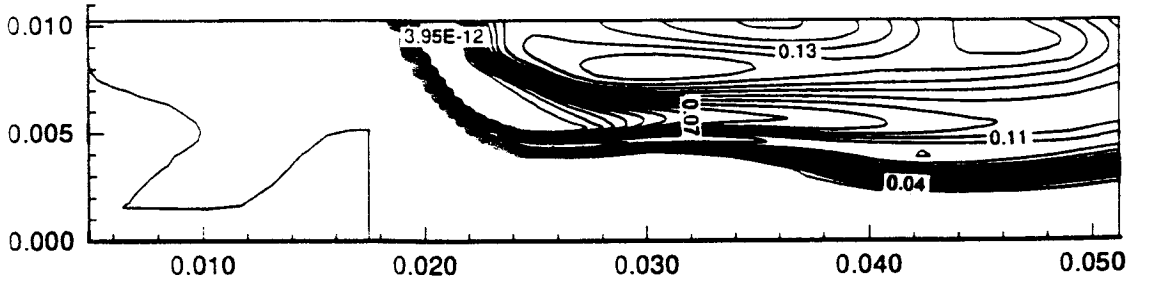

b. Edge of injector port.

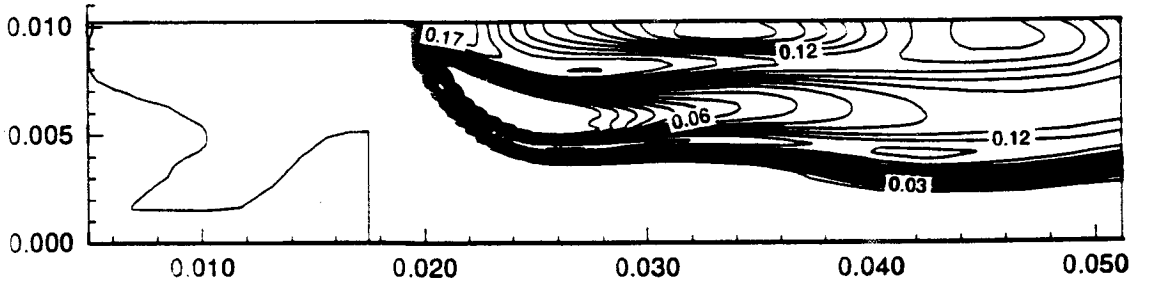

c. Between edge of injector port and injector slice symmetry boundary.

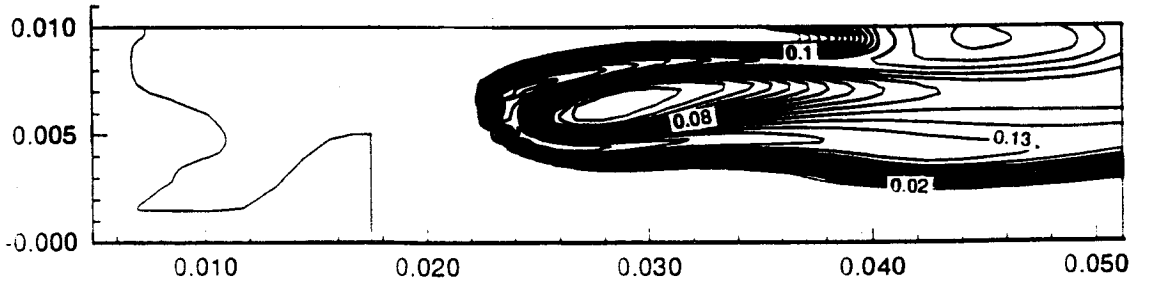

d. Injector slice symmetry boundary.

Figure 14: The OH mass fraction contours for a series of θ cross-planes.

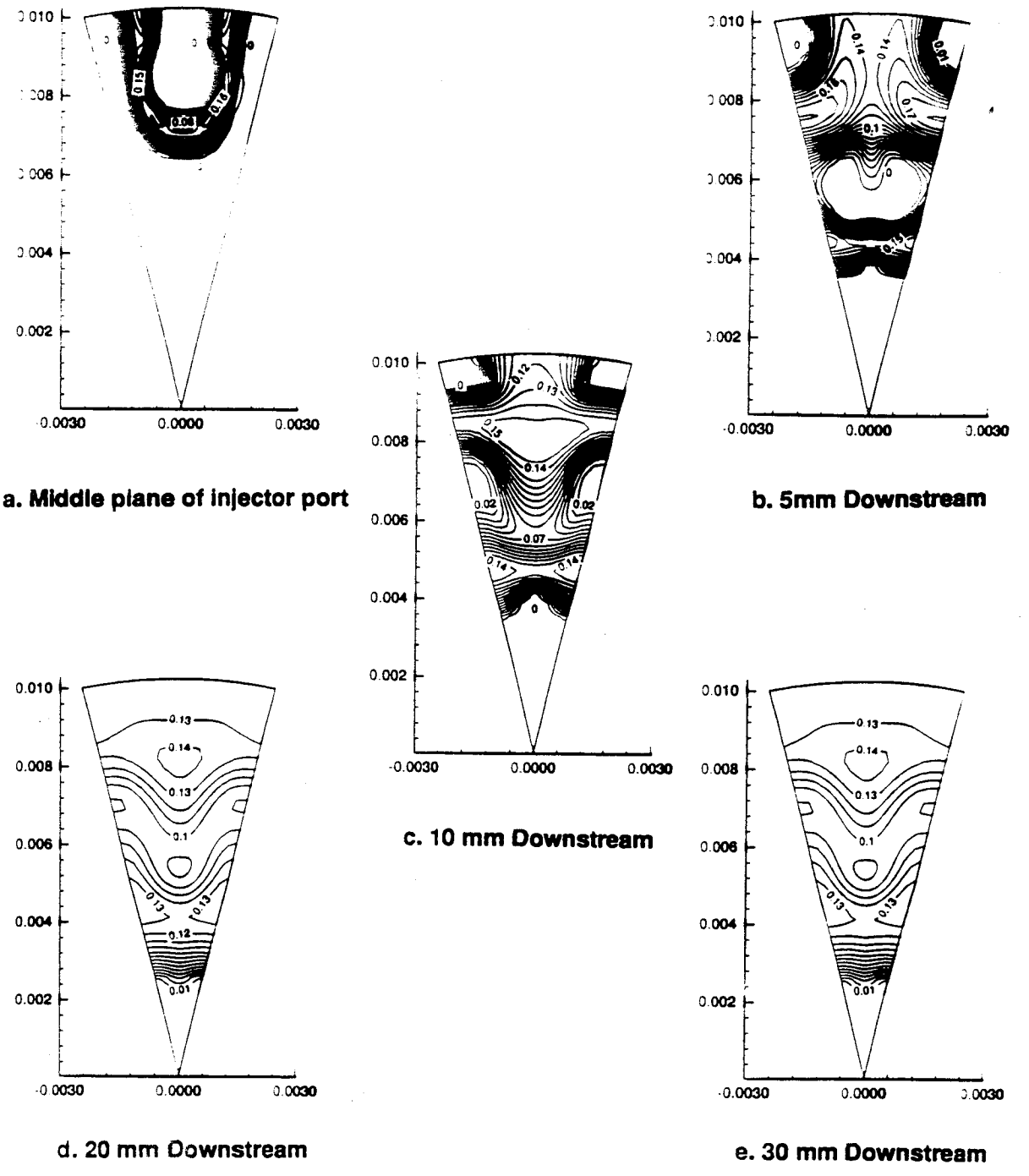

Figure 15: The OH mass fraction contours at five axial cross-sections.

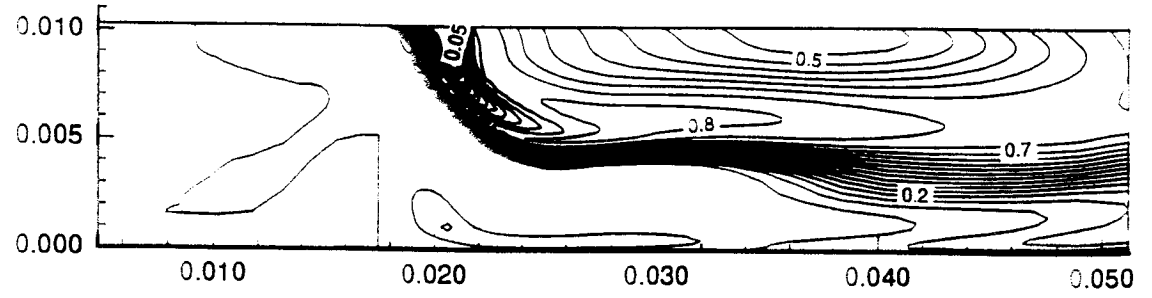

a. Symmetry plane of injector port.

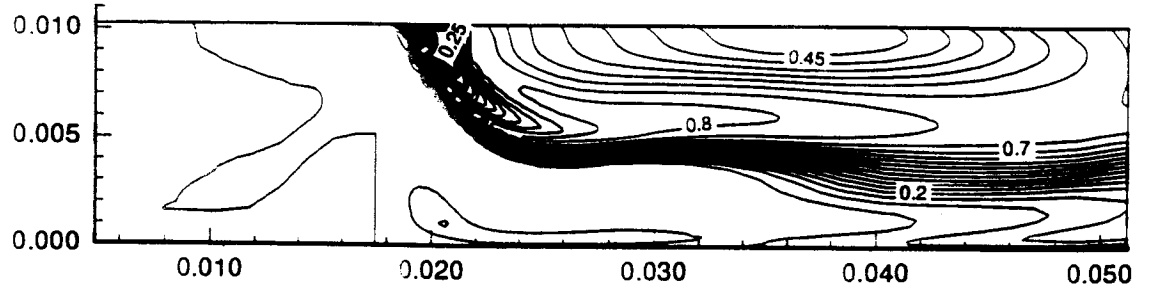

b. Edge of injector port.

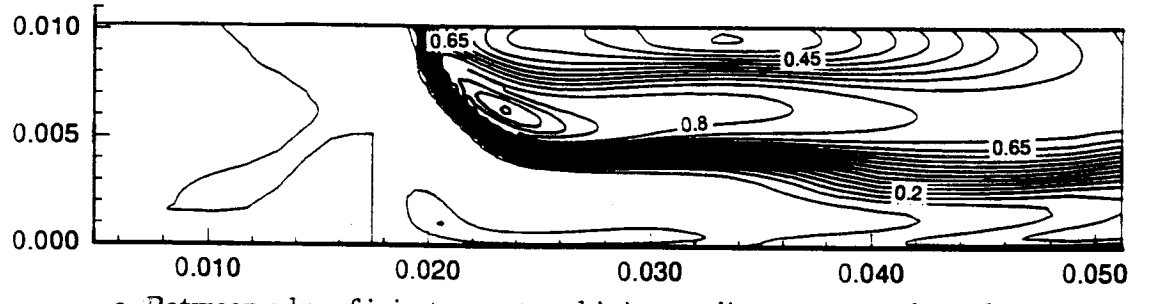

c. Between edge of injector port and injector slice symmetry boundary.

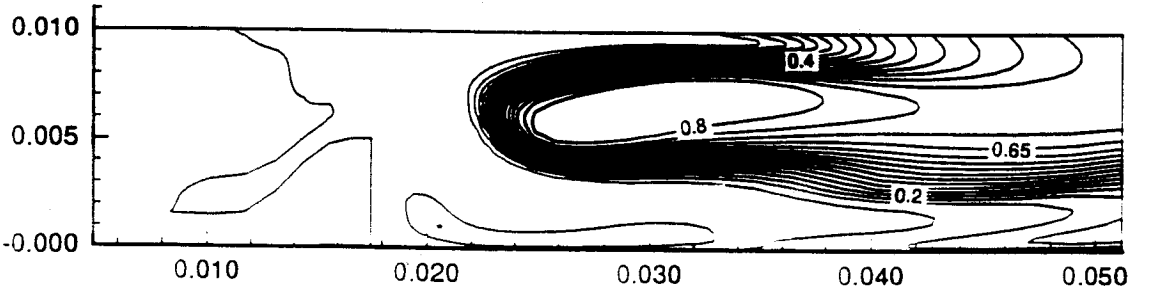

d. Injector slice symmetry boundary.

Figure 16: Water vapor mass fraction contours for a series of θ cross-planes.

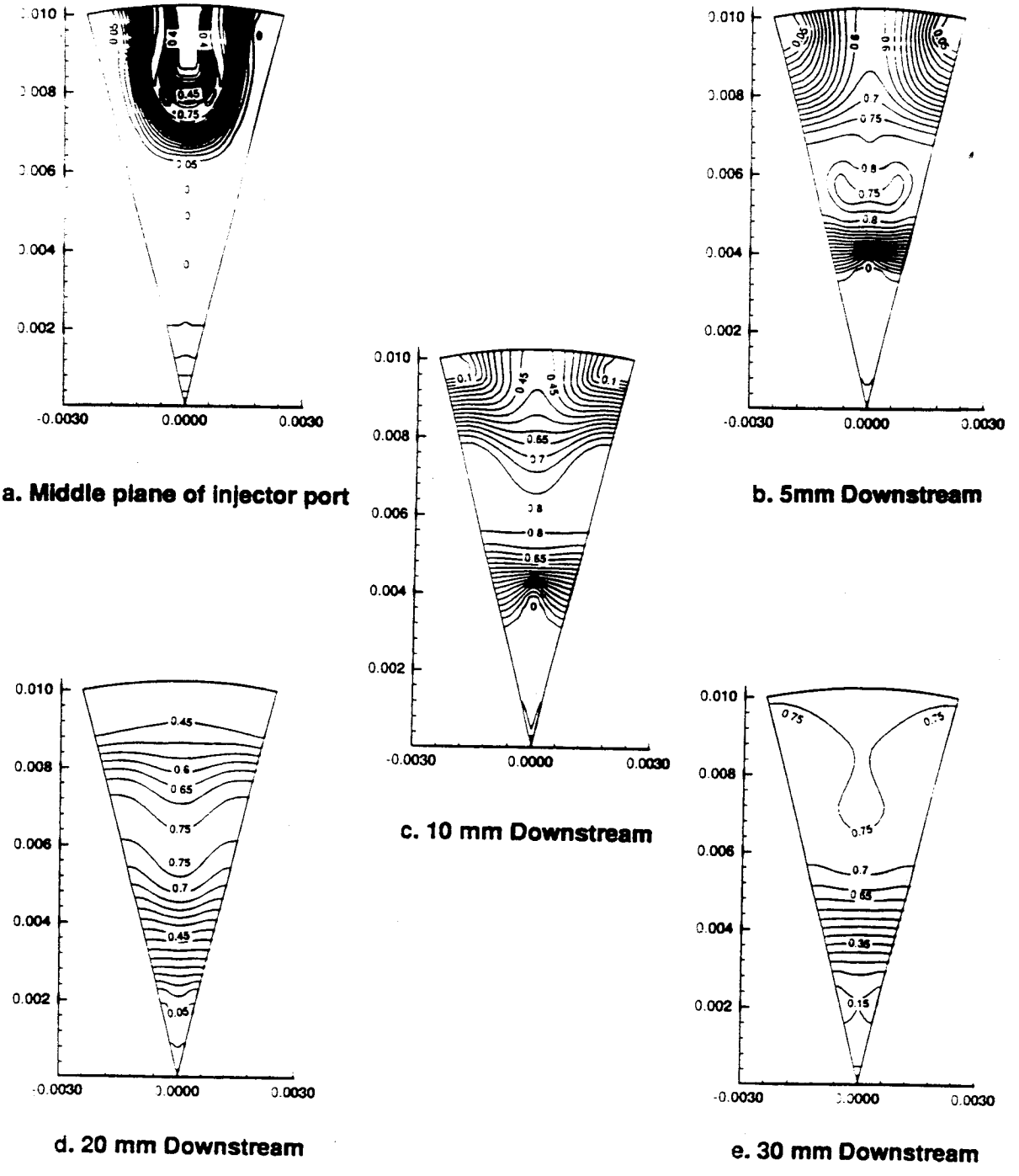

Figure 17: Water vapor mass fraction contours at five axial cross-sections.

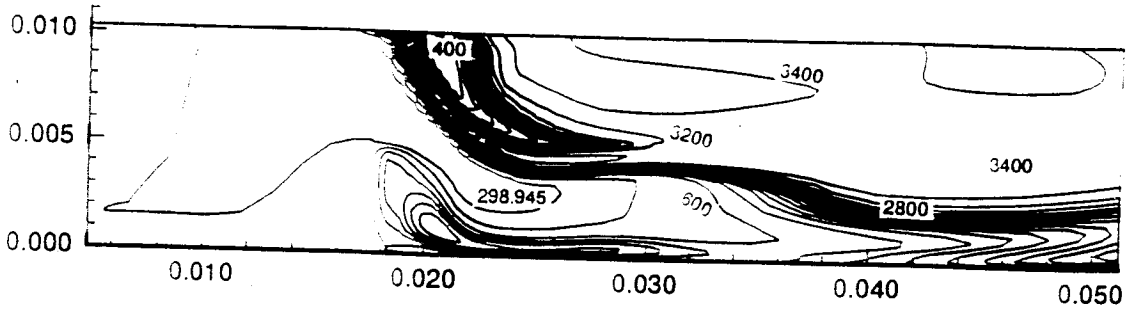

a. Symmetry plane of injector port.

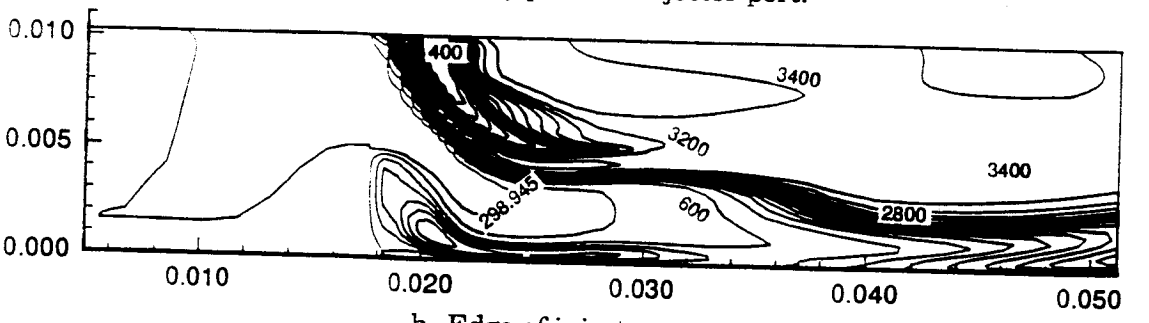

b. Edge of injector port.

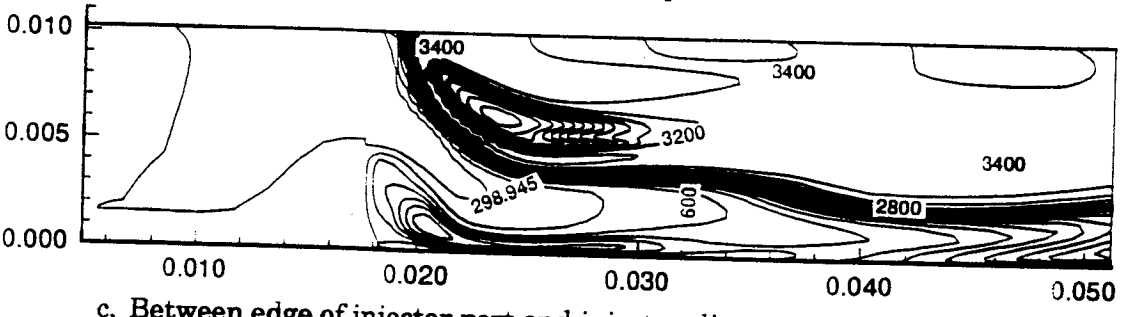

c. Between edge of injector port and injector slice symmetry boundary.

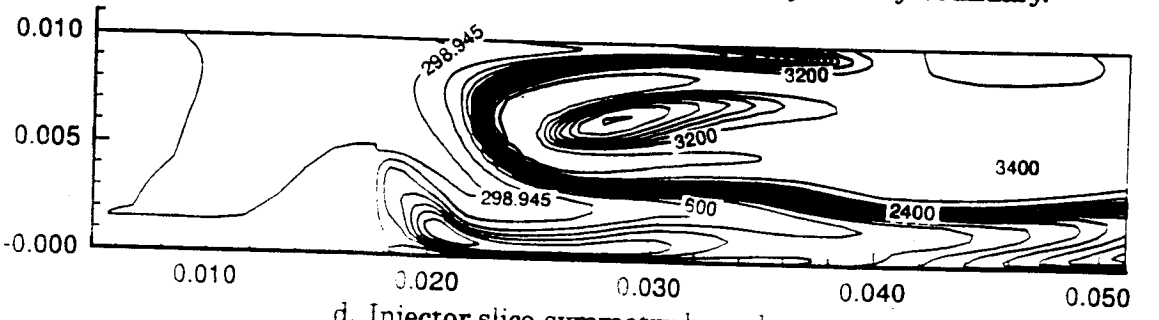

d. Injector slice symmetry boundary.

Figure 18: Temperature contours for a series of θ cross-planes.

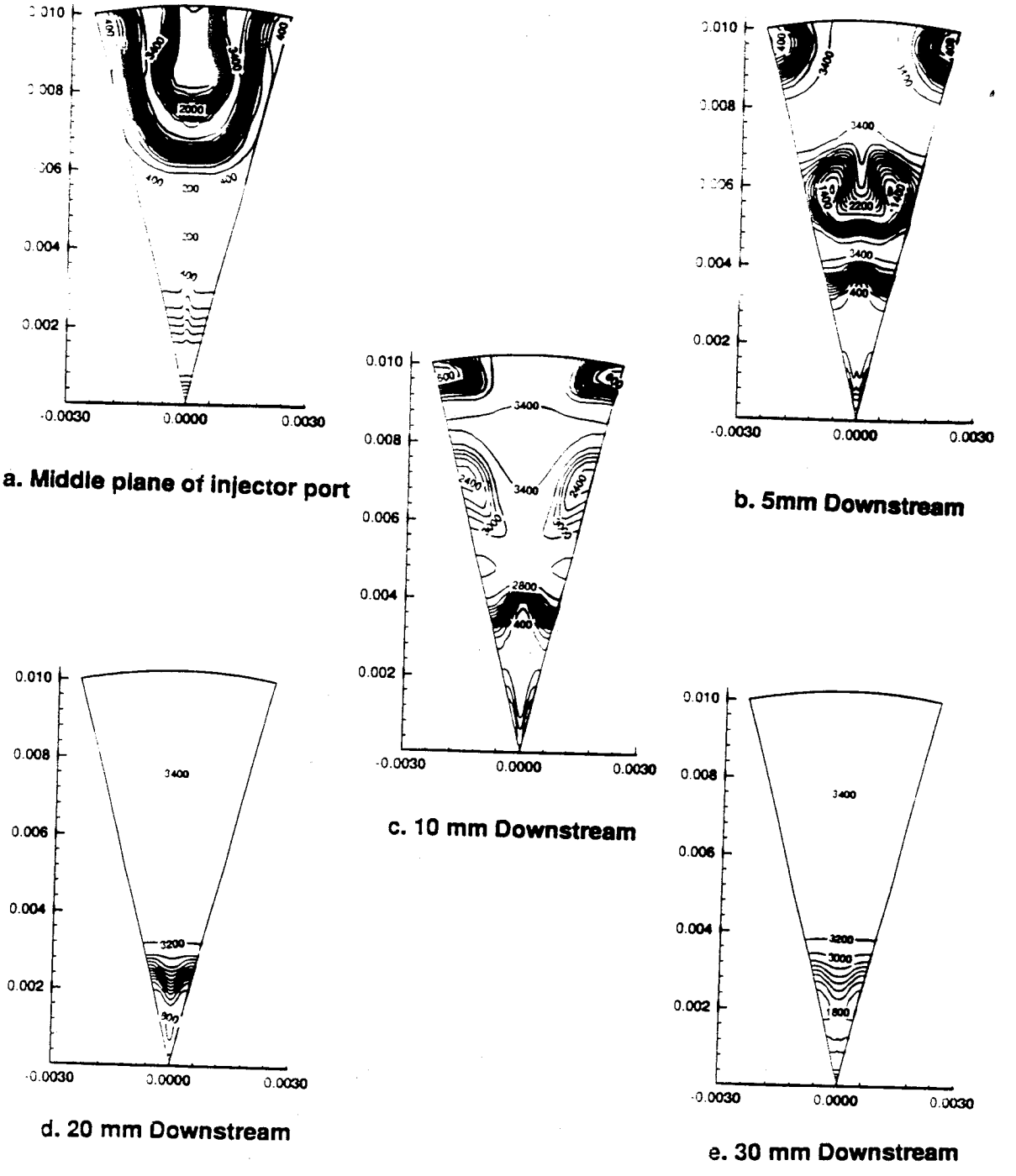

Figure 19: Temperature contours at five axial cross-sections.

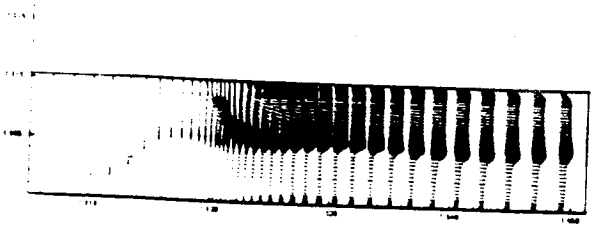

Figure 20a: Velocity vectors for transverse hydrogen injection into uniform oxygen flow. Tangential plane bisecting a hydrogen jet.

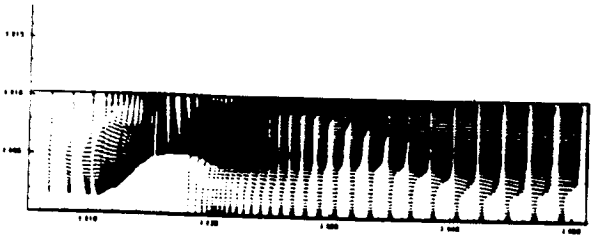

Figure 20b: Velocity vectors for transverse injection of hydrogen and oxygen. Tangential plane bisecting a hydrogen jet.

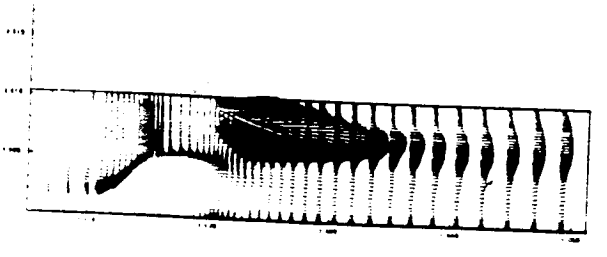

Figure 20c: Velocity vectors for transverse injection of hydrogen and oxygen. Tangential plane bisecting an oxygen jet.

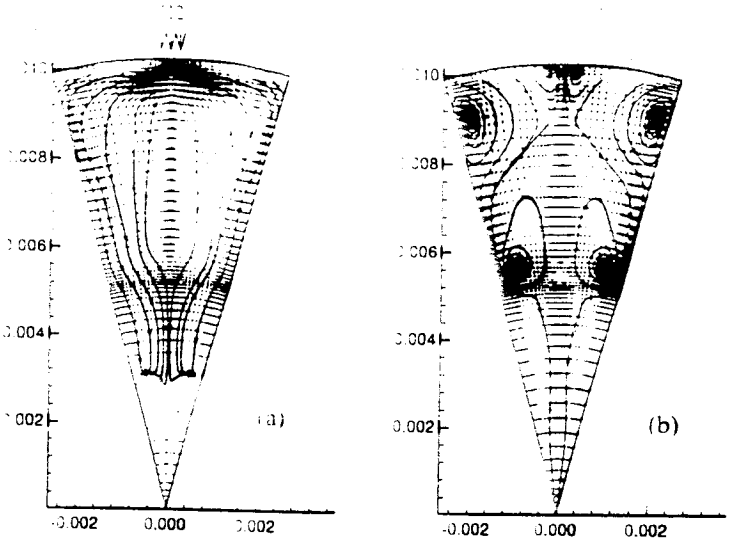

Figure 21: Transverse hydrogen and oxygen injection streamlines at two axial locations: a. Bisecting hydrogen jet; b. 5 mm downstream of H_2 jet.

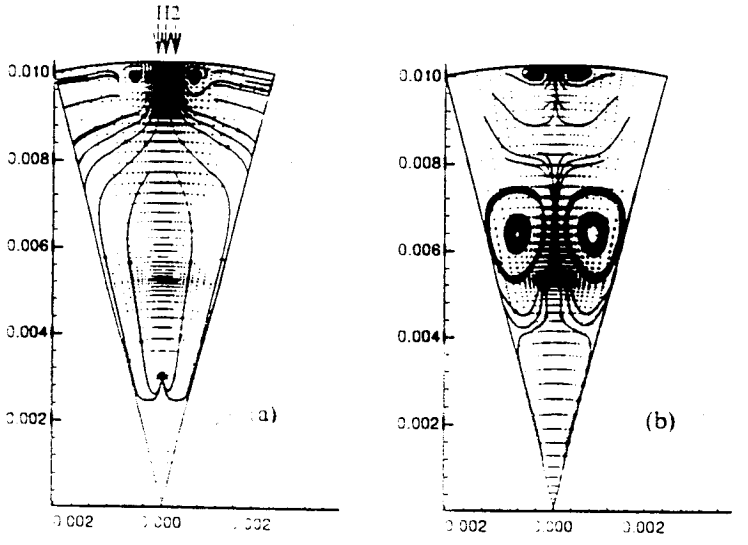

Figure 22: Transverse hydrogen injection into oxygen flow streamlines at two axial locations: a. Bisecting hydrogen jet; b. 5 mm downstream of H_2 jet.

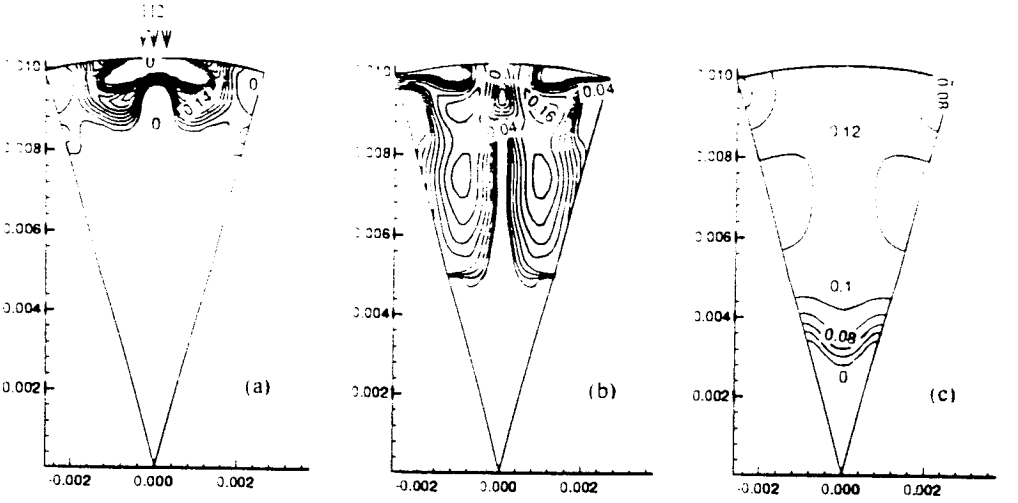

Figure 23: OH mass fractions for transverse hydrogen/oxygen injection on several axial planes: a. Bisecting H_2 jet; b. 5 mm downstream of H_2 jet; c. 30 mm downstream of H_2 jet.

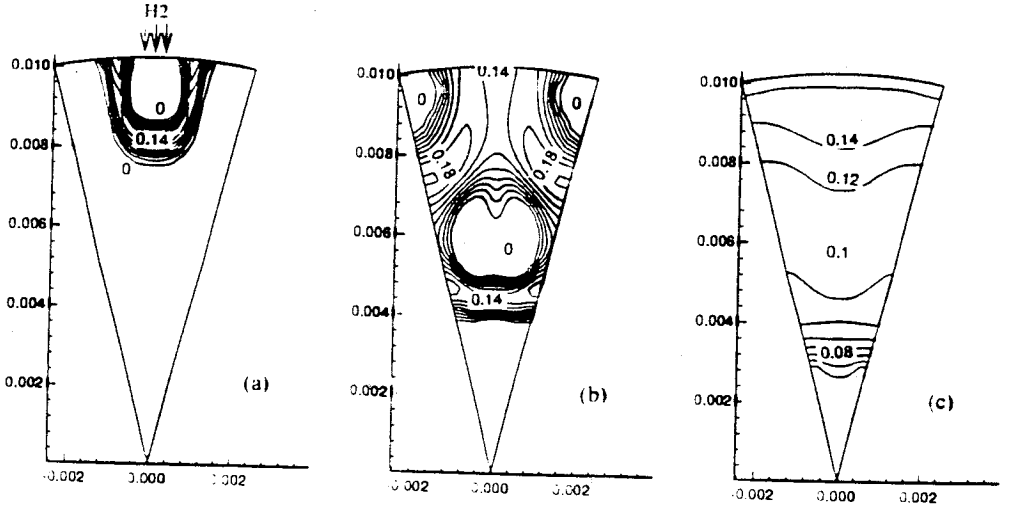

Figure 24: OH mass fractions for transverse hydrogen injection into oxygen on several axial planes: a. Bisecting H_2 jet; b. 5 mm downstream of H_2 jet; c. 30 mm downstream of H_2 jet.

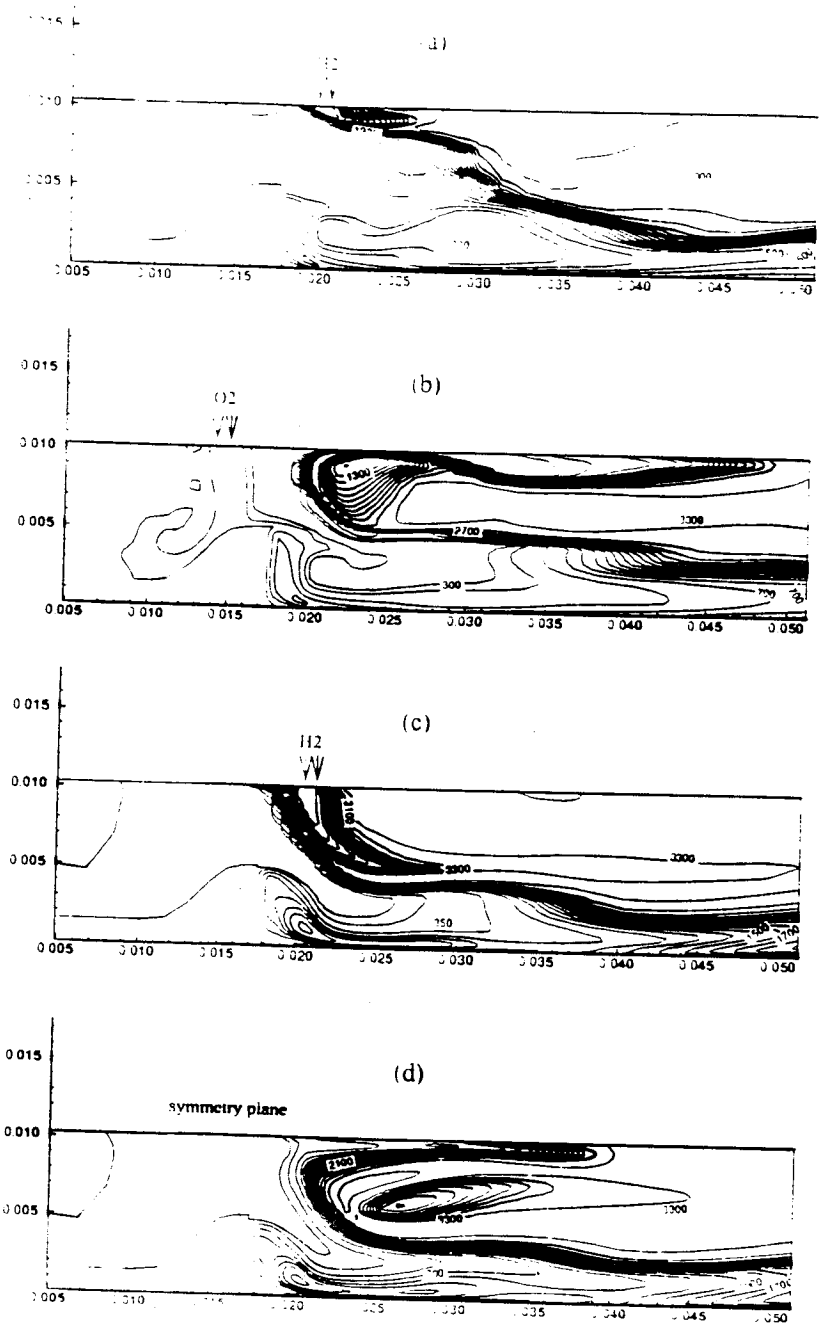

Figure 25: Temperature contours for several tangential cross-sectional planes: a. Transverse hydrogen and oxygen injection in plane bisecting H_2 jet; b. Bisecting O_2 jet; c. Only transverse hydrogen injection into axial oxygen flowfield in plane bisecting hydrogen jet; d. Symmetry plane between hydrogen jets.

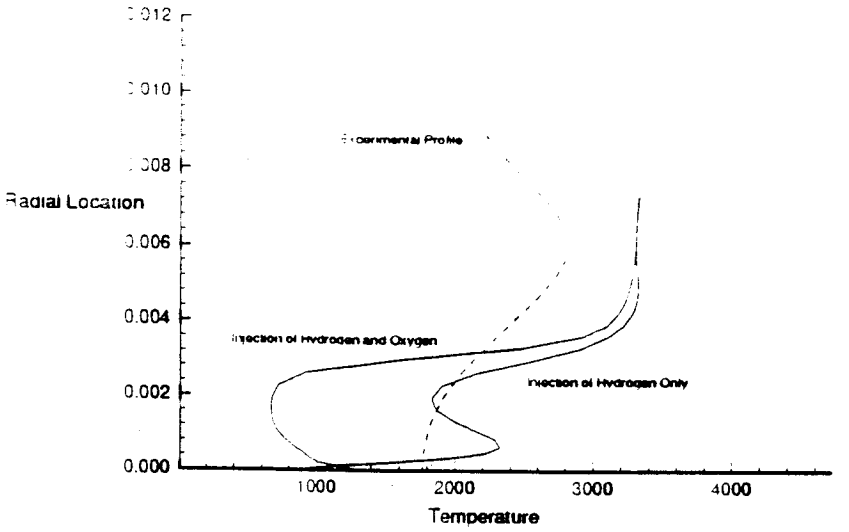

Figure 26: Comparison of circumferentially averaged temperature at exit plane as a function of radial location. Both computational solutions are compared with experimental data from NASA LeRC.

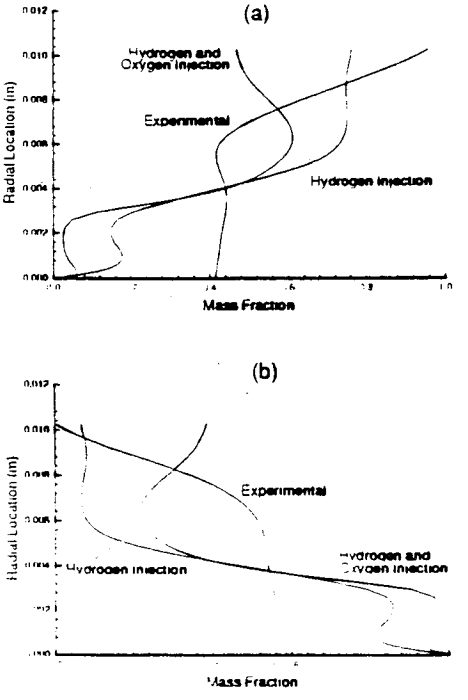

Figure 27: Comparison of circumferentially averaged species mass fractions at exit plane as a function of radial location. Both computational solutions are compared with experimental data from NASA LeRC: a. Water mass fractions; b. Oxygen mass fractions.

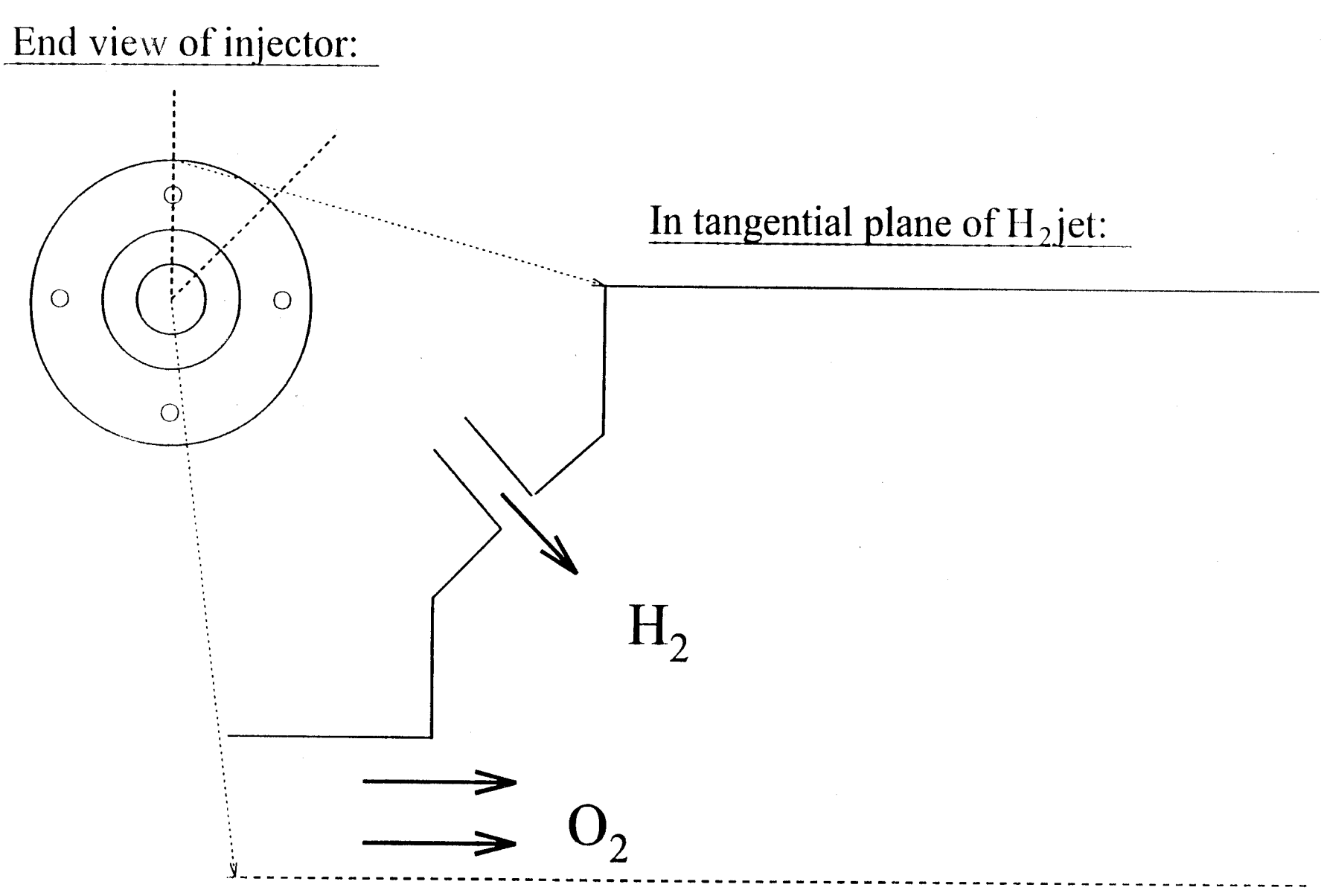

Figure 28: Schematic of impinging gas/gas injector.

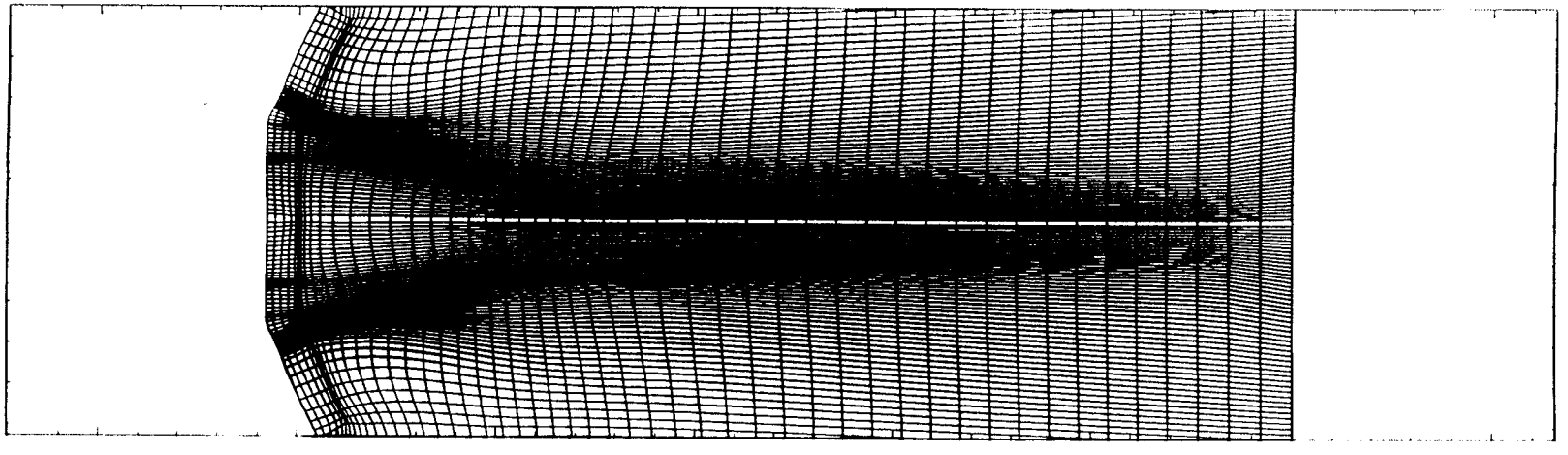

Figure 29: Cross-sectional grid of NASA LeRC impinging gas/gas geometry.

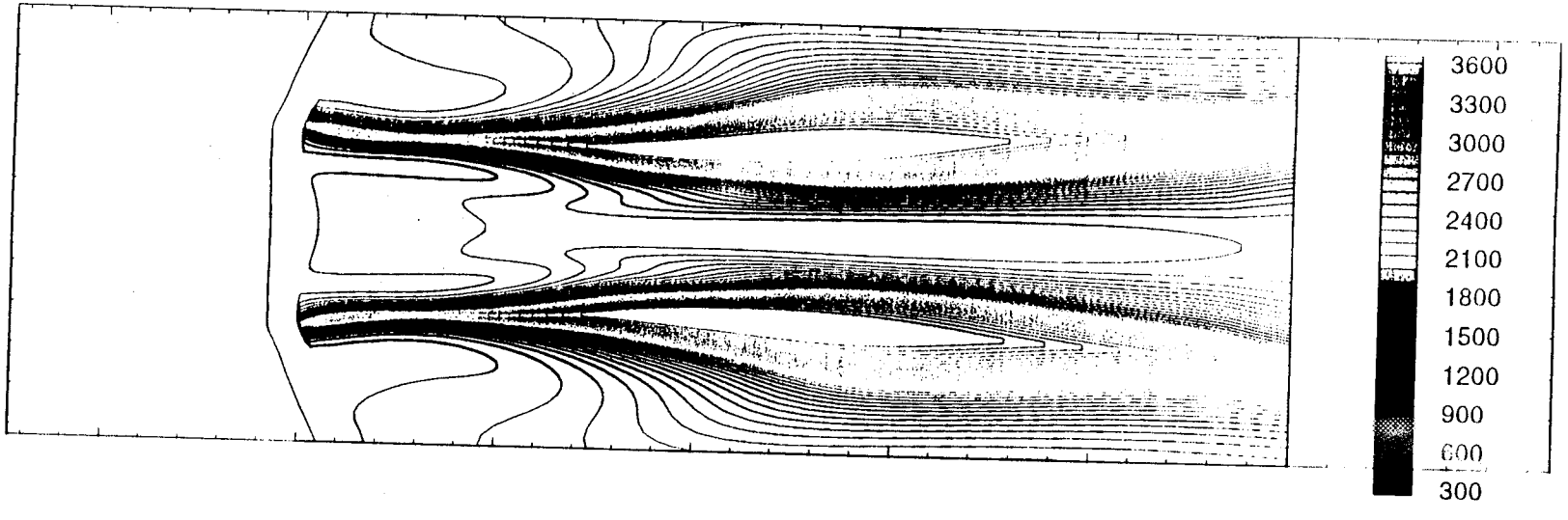

Figure 30: Temperature contours for NASA LeRC impinging gas/gas geometry.

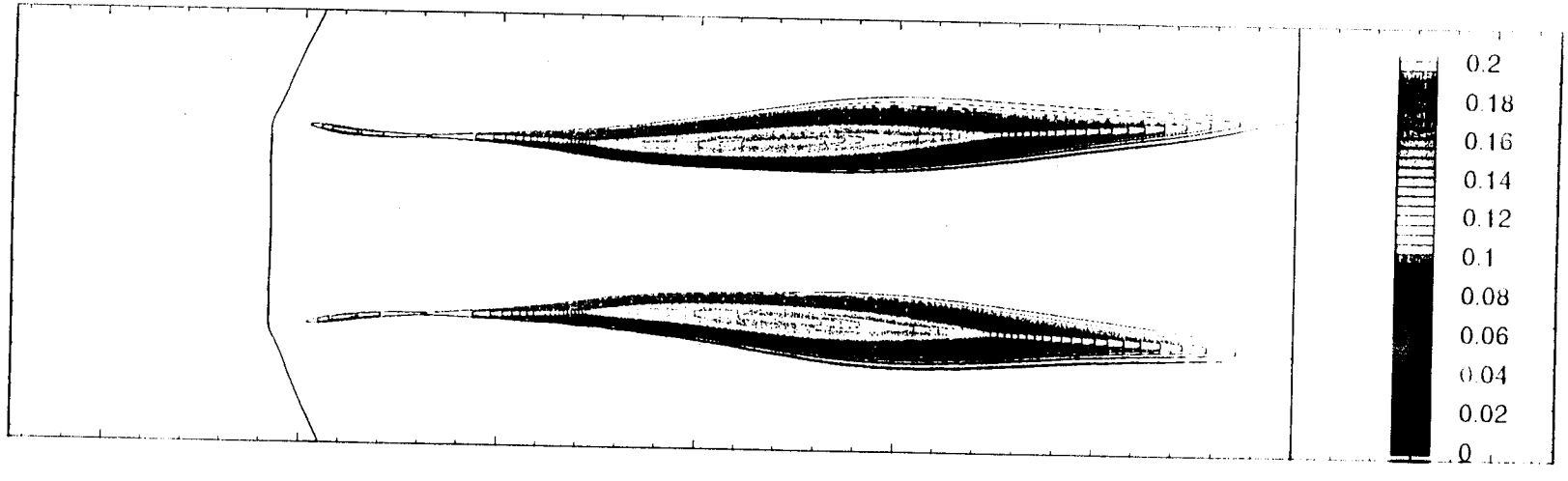

Figure 31: OH mass fraction contours for NASA LeRC impinging gas/gas geometry.